

Structure and Interactions of the Human Programmed Cell Death 1 Receptor*[‡]

Received for publication, December 21, 2012, and in revised form, February 11, 2013. Published, JBC Papers in Press, February 15, 2013, DOI 10.1074/jbc.M112.448126

Xiaoxiao Cheng^{†§1}, Vaclav Veverka^{¶1}, Anand Radhakrishnan^{**}, Lorna C. Waters[¶], Frederick W. Muskett[¶], Sara H. Morgan^{‡§}, Jiandong Huo^{‡§}, Chao Yu^{‡§}, Edward J. Evans^{‡§}, Alasdair J. Leslie[‡], Meryn Griffiths^{‡‡}, Colin Stubberfield^{‡‡}, Robert Griffin^{‡‡}, Alistair J. Henry^{‡‡}, Andreas Jansson^{§§}, John E. Ladbury^{§§}, Shinji Ikemizu^{¶¶}, Mark D. Carr^{¶2}, and Simon J. Davis^{‡§3}

From the [†]Radcliffe Department of Medicine and [§]Medical Research Council Human Immunology Unit, University of Oxford, John Radcliffe Hospital, Headington, Oxford OX3 9DU, United Kingdom, the [¶]Department of Biochemistry, University of Leicester, Leicester LE1 9HN, United Kingdom, the ^{||}Institute of Organic Chemistry and Biochemistry, Flemingovo Namesti 2, 166 10 Prague 6, Czech Republic, the ^{**}Department of Biochemistry and Molecular Biology, University of Texas M. D. Anderson Cancer Center, Houston, Texas 77030, ^{‡‡}UCB Pharma, Slough SL1 4EN, United Kingdom, the ^{§§}Systems Biology Research Centre, School of Life Sciences, University of Skövde, Box 408, Skövde, Sweden, and the ^{¶¶}Division of Structural Biology, Graduate School of Pharmaceutical Sciences, Kumamoto University, 5-1 Oe-honmachi, Kumamoto 862 0973, Japan

Background: The inhibitory leukocyte receptor PD-1 binds two ligands, PD-L1 and PD-L2.

Results: Nuclear magnetic resonance analysis and rigorous binding and thermodynamic measurements reveal the structure of, and the mode of ligand recognition by, PD-1.

Conclusion: PD-L1 and PD-L2 bind differently to PD-1 and much more weakly than expected.

Significance: Potent inhibitory signaling can be initiated by weakly interacting receptors.

PD-1, a receptor expressed by T cells, B cells, and monocytes, is a potent regulator of immune responses and a promising therapeutic target. The structure and interactions of human PD-1 are, however, incompletely characterized. We present the solution nuclear magnetic resonance (NMR)-based structure of the human PD-1 extracellular region and detailed analyses of its interactions with its ligands, PD-L1 and PD-L2. PD-1 has typical immunoglobulin superfamily topology but differs at the edge of the GFCC' sheet, which is flexible and completely lacks a C'' strand. Changes in PD-1 backbone NMR signals induced by ligand binding suggest that, whereas binding is centered on the GFCC' sheet, PD-1 is engaged by its two ligands differently and in ways incompletely explained by crystal structures of mouse PD-1-ligand complexes. The affinities of these interactions and that of PD-L1 with the costimulatory protein B7-1, measured using surface plasmon resonance, are significantly weaker than expected. The 3–4-fold greater affinity of PD-L2 *versus* PD-L1 for human PD-1 is principally due to the 3-fold smaller dissociation rate for PD-L2 binding. Isothermal titration calorimetry revealed that the PD-1/PD-L1 interaction is entropically driven, whereas PD-1/PD-L2 binding has a large enthalpic component. Mathematical simulations based on the biophysical data and quantitative expression data suggest an unexpectedly limited contribution of PD-L2 to PD-1 ligation during interactions of

activated T cells with antigen-presenting cells. These findings provide a rigorous structural and biophysical framework for interpreting the important functions of PD-1 and reveal that potent inhibitory signaling can be initiated by weakly interacting receptors.

In recent years, PD-1 (programmed cell death 1) has emerged as one of the most important inhibitory molecules in the immune system. Its potent inhibitory activity became evident when mice ablated at the *Pdcd1* locus developed strain-specific autoimmunity: sporadic glomerulonephritis on a C57BL/6 background (1) and cardiomyopathy in BALB/c mice (2). Genetic studies in humans also emphasize its importance insofar as *PDCD1* gene polymorphisms were found to confer susceptibility to systemic lupus erythematosus, atopy, and rheumatoid arthritis (3–5). PD-1 is also responsible for the “exhausted” phenotype of antigen-specific T cells in animal models of chronic infection (6, 7) and in human immunodeficiency (8) and hepatitis (9, 10) virus infections (although the latter is disputed (11)). It has also been implicated in the *de novo* generation of regulatory T cells (12). Such effects have made PD-1 one of the most actively studied therapeutic targets in cancer immunotherapy; presently, four anti-PD-1 antagonists are in clinical trials (reviewed in Ref. 13). It is suggested that PD-1 inhibits signaling, in T cells at least, by recruiting the phosphatase SHP-2 to TCR⁴ microclusters during the early stages of immunological synapse formation, where it blocks ongoing TCR signaling (14).

* This work was supported by the Wellcome Trust, the United Kingdom Medical Research Council, UCB Celltech Ltd., and a grant from the G. Harold and Leila Y. Mathers Charitable Foundation (to J. E. L.).

✂ Author's Choice—Final version full access.

[‡] This article contains supplemental Experimental Procedures and Table S1. The atomic coordinates and structure factors (code 2M2D) have been deposited in the Protein Data Bank (<http://www.pdb.org/>).

¹ Both authors contributed equally to this work.

² To whom correspondence may be addressed. E-mail: mdc12@le.ac.uk.

³ To whom correspondence may be addressed. E-mail: simon.davis@imm.ox.ac.uk.

⁴ The abbreviations used are: TCR, T cell receptor; DC, dendritic cell; hPD-1, hPD-L1, and hPD-L2, human PD-1, PD-L1, and PD-L2, respectively; mPD-1, mPD-L1, and mPD-L2, mouse PD-1, PD-L1, and PD-L2, respectively; RU, response units; ITC, isothermal titration calorimetry; PDB, Protein Data Bank; SPR, surface plasmon resonance; PE, phycoerythrin.

Structure and Interactions of PD-1

PD-1 expression is induced upon the activation of CD4⁺ T cells, CD8⁺ T cells, NKT cells, B cells, and monocytes (15), whereupon it binds two distinct ligands, PD-L1 (B7-H1 or CD274 (16, 17)) and PD-L2 (B7-DC (18, 19)). PD-L1 is both constitutively and inducibly expressed by T and B cells, dendritic cells (DCs), macrophages, mesenchymal stem cells, and bone marrow-derived mast cells and on nonhematopoietic cells; PD-L2 expression is up-regulated on DCs, macrophages, and mast cells (reviewed in Ref. 15). PD-1 is a monomeric type I surface glycoprotein consisting of a single V-set immunoglobulin superfamily (IgSF) domain attached to a transmembrane domain and a cytoplasmic domain with two tyrosine-based signaling motifs. PD-1 is often assigned to the CD28 receptor family, mostly on the basis of functional similarities (e.g. see Ref. 20). However, PD-1 actually shares more structural homology with antigen receptors and CD8 and can be considered to be intermediate between the antigen receptors and CD28 family proteins, suggesting that a PD-1-like protein was a precursor of IgSF family signaling receptors (21). Like the ligands of CD28 and CTLA-4, PD-L1 and PD-L2 are B7 family proteins comprised of tandem V-set and C1-set IgSF domains. In addition to PD-1, PD-L1 binds B7-1, one of the ligands of CD28 and CTLA-4 (22, 23), potentially interlocking the PD-1 and CD28/CTLA-4 signaling pathways. Structures of mouse PD-1 complexed with human PD-L1 (24) and mouse PD-L2 (25) revealed that these proteins interact largely orthogonally via their GFCC'C" β -sheets. The complex of mouse PD-1 and human PD-L1 (24) is highly reminiscent of V-set domain dimers in antigen receptors, suggesting how in *trans* interacting receptors could have evolved into in *cis* interacting IgSF dimers, or *vice versa* (21, 26).

Despite its considerable immunotherapeutic potential, we know relatively little about the structure and interactions of human PD-1. There are no published structures of ligand-bound or unbound forms of the receptor, and whereas relatively high avidities have been measured for the interactions of bivalent forms of PD-1 with its ligands (reviewed in Ref. 15), there have been no systematic measurements of the true affinities. Here, we present the structure of a soluble form of human PD-1 and map its interactions with PD-L1 and PD-L2 using nuclear magnetic resonance (NMR)-based approaches. The new structure helps to account for the distinct affinity and thermodynamic properties of PD-1 binding to PD-L1 and PD-L2. Measurements of the human and mouse affinities suggest that potent inhibitory signaling can be mediated by surprisingly weak interactions. Finally, we use simulations of signaling complex formation to explore the reasons why PD-1 might have two distinct ligands and to gauge the impact of PD-L1 binding to B7-1.

EXPERIMENTAL PROCEDURES

Expression and Purification of PD-1 and Its Ligands—The extracellular region of the mature form of human PD-1 (hPD-1; residues 14–130), with a Met added to the N terminus and a Cys to Ser mutation introduced at position 73 to aid expression and folding, was expressed in the form of untagged protein in inclusion bodies in *Escherichia coli* BL21 (DE3) pLysS cells using a modified pET vector (Novagen). Uniformly ¹⁵N-, ¹⁵N/

¹³C-, and ²H/¹³C/¹⁵N-labeled hPD-1 was produced from cells grown in minimal medium containing [¹⁵N]ammonium sulfate and D-[¹³C]glucose, if required, as the sole nitrogen and carbon sources, and 100% D₂O when appropriate. Refolding conditions were determined using the iFOLD System 2 Screen (Merck). The hPD-1-expressing cells were resuspended in 50 mM Tris-HCl, 50 mM NaCl, 1 mM Tris(hydroxypropyl)phosphine, 0.5 mM EDTA, 5% glycerol, pH 8.0, before passing twice through a cell disrupter at 30,000 p.s.i. The lysate was made up to 125 mM with non-detergent sulfobetaine 201 (Sigma) and mixed. The hPD-1-containing inclusion bodies were washed once with the above buffer containing 125 mM non-detergent sulfobetaine 201 and then three times with the same buffer without non-detergent sulfobetaine 201. Inclusion bodies were solubilized in 50 mM Tris-HCl, 200 mM NaCl, 2 mM EDTA, 6 M guanidine HCl, pH 8.0. hPD-1 was subsequently efficiently refolded by rapid dilution into 50 mM HEPES, pH 7.5, 500 mM L-arginine, 9 mM glutathione, 1 mM glutathione disulfide, 24 mM NaCl, 1 mM KCl. The refolding mixture was then concentrated by tangential flow filtration, and the refolded protein was purified using a 16/60 Superdex 200 gel filtration column (GE Healthcare). The authenticity of the refolded hPD-1 material was assessed by the comparison of its ¹H NMR spectrum with the data obtained for the protein produced in a eukaryotic expression system. Unlabeled, soluble His₆-tagged, and biotinylatable forms of human and mouse PD-L1 (hPD-L1 and mPD-L1) and PD-L2 (hPD-L2 and mPD-L2) were produced via stable expression in Chinese hamster ovary (CHO) cells, using approaches used previously (27–29).

NMR Spectroscopy—NMR spectra were acquired from 0.35-ml samples of 0.5 mM free hPD-1 and 0.2 mM hPD-1·hPD-L1 or hPD-1·hPD-L2 complex in a 25 mM sodium phosphate, 100 mM sodium chloride buffer at pH 6.4, containing 5% D₂O, 95% H₂O. All of the NMR data were collected at 25 °C on either 600- or 800-MHz Bruker Avance spectrometers equipped with triple resonance (¹⁵N/¹³C/¹H) cryoprobes. A series of double and triple resonance spectra were recorded to determine essentially complete sequence-specific resonance assignments for hPD-1, as described previously (30–32). ¹H-¹H distance constraints required to calculate the structure of hPD-1 were derived from NOEs identified in NOESY, ¹⁵N/¹H NOESY-HSQC, and ¹³C/¹H HSQC-NOESY spectra, which were acquired with an NOE mixing time of 100 ms. The specific binding of either hPD-L1 or hPD-L2 to hPD-1 was monitored by changes induced in the positions of signals of ²H/¹³C/¹⁵N-labeled hPD-1 in three-dimensional TROSY-HNCO spectra (33). Residues involved in forming stable backbone hydrogen bonds were identified by monitoring the rate of backbone amide exchange in two-dimensional ¹⁵N/¹H HSQC spectra of hPD-1 dissolved in D₂O.

Structural Calculations—The family of converged hPD-1 structures was initially calculated using Cyana 2.1 (34), as described previously (35). The combined automated NOE assignment and structure determination protocol was used to automatically assign the NOE cross-peaks identified in two-dimensional NOESY and three-dimensional ¹⁵N- and ¹³C-edited NOESY spectra and to produce preliminary structures. In addition, backbone torsion angle constraints, generated from

assigned chemical shifts using the program TALOS+ (36), and hydrogen bond constraints involving residues with slowly exchanging amide protons were included in the calculations. Subsequently, five cycles of simulated annealing combined with redundant dihedral angle constraints (Redac) (37) were used to produce the 52 converged hPD-1 structures with no significant restraint violations (distance violations $<0.2 \text{ \AA}$ and dihedral angle violations $<5^\circ$), which were further refined with two cycles of restrained molecular dynamics simulated annealing using AMBER (38). Initial energy minimization (2000 steps) was followed by 20 ps of simulated annealing in vacuum and three cycles of 20-ps simulated annealing using a generalized Born solvent model (39) with force constants of $30 \text{ kcal mol}^{-1} \text{ \AA}^2$ for distance constraints (NOEs, hydrogen bonds, disulfide bridge), $1000 \text{ kcal mol}^{-1} \text{ rad}^{-2}$ for dihedral angle constraints, and $10 \text{ kcal mol}^{-1} \text{ rad}^{-2}$ for chirality constraints. The 35 structures with the lowest AMBER energy and with no distance constraint violation greater than 0.18 \AA and dihedral angle constraint violation greater than 5° were selected. Analysis of the family of structures obtained was carried out using the programs Molmol, Molprobit, and PyMOL (40–42).

Analysis of NMR Binding Data—The minimal shift approach (43–45) was used to assess the changes in the positions of hPD-1 backbone signals (H^N , N, and C') resulting from the binding of hPD-L1 or hPD-L2. A detailed description of the exact procedure is published (35). To facilitate the identification of ligand binding sites on the surface of hPD-1, histograms of the actual and minimal combined shift *versus* the protein sequence were used to identify regions of the protein containing a number of significantly perturbed backbone signals. The affected residues within these regions were then assessed as possible interaction sites in the ligand-binding site by examination of the solution structure determined for hPD-1.

Surface Plasmon Resonance (SPR) Experiments—Binding experiments were carried out using surface plasmon resonance as implemented in the BiacoreTM 3000 (GE Healthcare). Affinity and kinetic analyses were performed at 37°C in HBS-EP buffer (25 mM HEPES, pH 7.4, 150 mM NaCl, 3.4 mM EDTA, and 0.005% surfactant P20; GE Healthcare). For experiments to determine the binding affinity of human and mouse PD-1 for their ligands, biotinylated soluble forms of human and mouse PD-L1 and PD-L2 or control biotinylated protein (CD4) were indirectly immobilized to the sensor surface of SA sensor chips (GE Healthcare) via streptavidin to levels of ~ 2000 response units (RU) as described previously (46). Soluble, monomeric forms of PD-1 were then injected over the immobilized ligands. Alternatively, human or mouse PD-1Fc fusion protein or control fusion protein (CD28Fc (47)) at $25 \mu\text{g/ml}$ in 10 mM sodium acetate, pH 4.5, was directly immobilized to the dextran matrix of research grade CM5 sensor chips (GE Healthcare) by amine coupling using the manufacturer's kit (GE Healthcare) and an activation time of 5 min, resulting in immobilization levels of ~ 4000 RU. In this case, His₆-tagged forms of hPD-L1 and hPD-L2 were injected over the immobilized PD-1Fc. For kinetic analyses in each orientation, the immobilization levels were lower, at ~ 500 – 1200 RU. Equilibrium binding analysis was undertaken as described (28, 29). Briefly, serial dilutions of hPD-L1 or hPD-L2 or of PD-1 monomer (released by thrombin

treatment of PD-1Fc fusion protein (47)) were injected simultaneously over flow cells containing directly immobilized PD-1Fc (or CD28Fc) or indirectly immobilized biotinylated hPD-L1 and hPD-L2 or control protein (CD4) at 25 and 37°C . Injections were of 1-min duration, at a buffer flow rate of $10 \mu\text{l/min}$, which was sufficient for binding to reach equilibrium. For the kinetic analyses, dissociation rates were measured as described (28, 29). The binding data were examined using BIAevaluation software (GE Healthcare), and affinity and kinetic parameters were derived using the curve fitting tools of Origin version 5.0 (MicroCal Software Inc., Northampton, MA).

Isothermal Titration Calorimetry (ITC)—ITC experiments were performed using the MCS or VP-ITC systems (MicroCal Software Inc.) as described (48, 49). In a typical experiment, hPD-L1 or hPD-L2 at 0.2 mM was added in 20 $15\text{-}\mu\text{l}$ injections to a 0.02 mM solution of human PD-1Fc in the 1.463-ml calorimeter cell at the temperatures indicated. The resulting data were fitted as described (48) after subtracting the heats of dilution resulting from the addition of hPD-L1 or hPD-L2 to buffer and buffer to hPD-1Fc, determined in separate control experiments. Titration data were fitted using a non-linear least squares curve-fitting algorithm with three floating variables: stoichiometry, association constant (K_a), and change of enthalpy on binding (ΔH_{obs}). All binding data were analyzed by fitting the binding isotherm to a single independent binding site model using Origin software provided with the ITC. ITC allows for the complete thermodynamic characterization of an interaction based on the relationship, $\Delta G = -RT \times \ln(K_a) = \Delta H_{\text{obs}} - T\Delta S$, where R is the gas constant, T is the absolute temperature, and ΔG , ΔH_{obs} , and ΔS are the standard free energy, observed enthalpy, and entropy changes going from unbound to bound states, respectively. All experiments were done in triplicate.

Simulations of PD-1-PD-L1 and PD-1-PD-L2 Complex Formation—The theoretical framework used to simulate the interactions of human PD-1 with its ligands and of human PD-L1 with B7-1 is analogous to that used previously to analyze costimulatory interactions at the synaptic interface between a naive/activated T cell and an immature/mature DC (50, 51). A description of the model is given in the [supplemental Experimental Procedures](#). Parameter values for the molecular interactions and the expression levels used in the simulations are taken from the present study, whereas the values for diffusion and mobility used are those for costimulatory molecules (50).

RESULTS

Human PD-1 Extracellular Region Structure Determination

The authenticity of refolded, $^{13}\text{C}/^{15}\text{N}$ -labeled hPD-1 produced in bacteria (see “Experimental Procedures”) was confirmed by showing that its one-dimensional ^1H NMR spectra was essentially indistinguishable from that of deglycosylated hPD-1 expressed in Chinese hamster ovary cells (data not shown). The thermal stability of this material, tested by differential scanning fluorimetry (data not shown), was sufficient for the acquisition of multiple three-dimensional NMR experiments at 25°C . Comprehensive sequence-specific

Structure and Interactions of PD-1

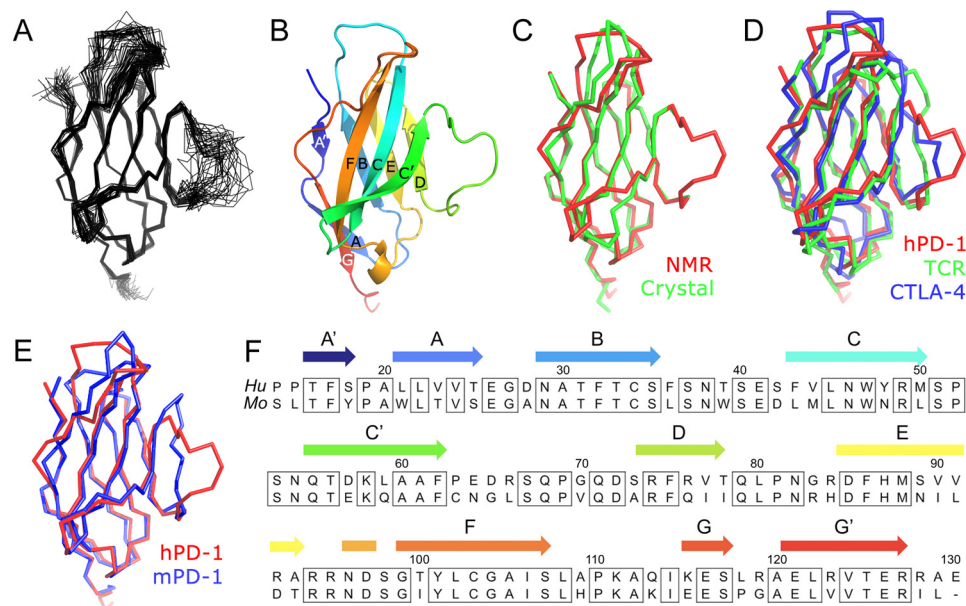


FIGURE 1. Solution structure of the extracellular domain of human PD-1. *A*, best fit superposition of the protein backbone for the 35 converged structures obtained for hPD-1. *B*, ribbon representation of the backbone topology of the structure closest to the mean, in the same orientation. *C*, comparison of the NMR-based (red) and crystal (green; PDB accession number 3RRQ) structures of hPD-1. *D*, comparison of the structures of hPD-1, TCR δ V-domain (PDB accession number 3OMZ), and CTLA-4 (PDB accession number 3OSK). *E*, comparison of the backbone topologies of human (red) and mouse (PDB accession number 1NPU; blue) PD-1. *F*, structure-based alignment of the sequences of human (*Hu*) and mouse (*Mo*) PD-1 (mature polypeptide numbering).

TABLE 1
NMR constraints and structural statistics for PD-1

No. of constraints used in structural calculations	
Intraresidue NOEs	399
Sequential NOEs ($i, i + 1$)	432
Medium range NOEs ($i, i + 1 \leq 4$)	134
Long-range NOEs ($i, i \geq 5$)	734
Torsion angles	297 (90 F, 90 Y, 117 W)
Backbone hydrogen bonds	132 (33 hydrogen bonds)
Disulfide bond	6 (Cys ⁵⁴ --Cys ¹²³)
Violations and energies	
Maximum distance violation	0.18 Å
Maximum dihedral angle violation	4.9°
Number of distance violations >0.15 Å	7
Number of dihedral angle violations >5°	0
Mean AMBER energy	-4314.4 kcal mol ⁻¹
Mean constraint energy	5.2 kcal mol ⁻¹
Deviations for idealized geometry	
Bond lengths	$96.8 \times 10^{-4} \pm 0.6 \times 10^{-4}$ Å
Bond angles	1.89 ± 0.02 °
Root mean square deviations from mean structure	
Backbone heavy atoms	1.52 ± 0.31 Å
Backbone heavy atoms (structured region) ^a	0.55 ± 0.12 Å
All heavy atoms	2.27 ± 0.30 Å
All heavy atoms (structured region) ^a	1.38 ± 0.18 Å
Ramachandran plot (F and Y angle distribution (%))^b	
Residues in favored regions	96.3 (3911/4060)
Residues in additional allowed regions	99.9 (4057/4060)

^a Values for the regions adopting regular secondary structure.

^b Determined using the program Molprobity.

backbone and side chain resonance assignments were obtained using established triple resonance experiments (30–32). Resonance assignments obtained for protons were >96.4% complete, with only the two N-terminal residues (Met and Pro) and parts of several aromatic side chains remaining unassigned. The completeness of the ¹⁵N, ¹³C, and ¹H resonance assignments allowed automated assignment of the NOEs identified in three-dimensional ¹⁵N/¹H NOESY-HSQC, in ¹³C/¹H HSQC-NOESY, and in the aromatic to aliphatic region of two-dimensional NOESY spectra

using the CANDID protocol implemented in Cyana (34). This yielded unique assignments for 94.9% (2702 of 2847) of the NOE peaks observed, providing 1561 non-redundant ¹H-¹H distance constraints. Fifty-two satisfactorily converged hPD-1 structures were obtained from 100 random starting conformations using 1879 NMR-derived structural constraints (~16 constraints/residue), which were further refined in AMBER by simulated annealing using a generalized Born solvent model (39). A final round of refinement yielded 35 structures with no distance violations of >0.18 Å (Fig. 1*a* and Table 1). The hPD-1 structures, NMR constraints, and resonance assignments have been deposited in the Protein Data Bank (PDB; accession number 2M2D) and BMRB database (accession number 18908).

Overall Structure and Comparison with Mouse Apo-PD-1

The structure shows that hPD-1, comprising residues 16–127 of the mature polypeptide, consists of a two-layer β sandwich with the topology of IgSF domains (*i.e.* two β sheets (GFCC' and ABED) stabilized by a disulfide bond (Cys³⁴–Cys¹⁰³; Fig. 1*B*). Following determination of our structure, the coordinates for an equivalent form of hPD-1 obtained crystallographically were deposited in the PDB (PDB accession number 3RRQ). The two structures exhibit a very high degree of similarity (Fig. 1*C*). Automated structure comparisons using DALI (52) identified antigen receptor variable domains and the extracellular V-set domain of CTLA-4 as the structures most similar to hPD-1, as expected (21). The only significant difference between hPD-1 and these receptors was the extra flexibility in the region flanked by the C' and D β strands (Fig. 1*D*). Detailed comparisons of human and mouse apo-PD-1 (53) reveal that although, overall, they are very similar (root mean square differences <1.30 Å for 104 C α atoms), there are two regions of significant local differences (Fig. 1*E*). First, Pro¹¹⁰

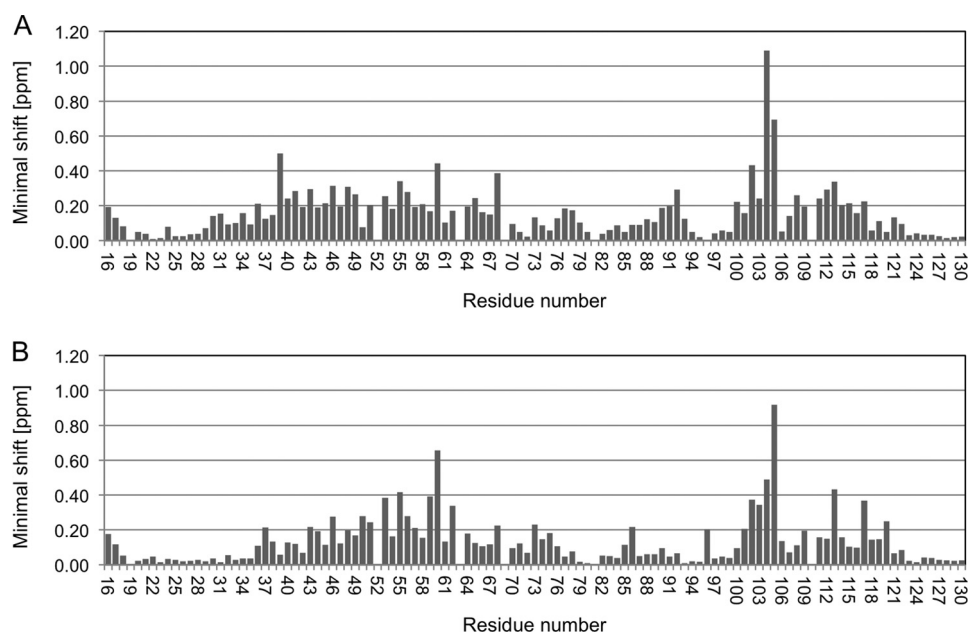


FIGURE 2. Minimal backbone chemical shift (^{15}N , ^{13}C , and $^1\text{H}^{\text{N}}$) change values observed for hPD-1 on hPD-L1 (A) or hPD-L2 (B) binding. The values were obtained by comparison of three-dimensional TROSY-HNCO spectra of the samples consisting of the free or hPD-L1/hPD-L2-bound $^2\text{H}/^{13}\text{C}/^{15}\text{N}$ -labeled hPD-1.

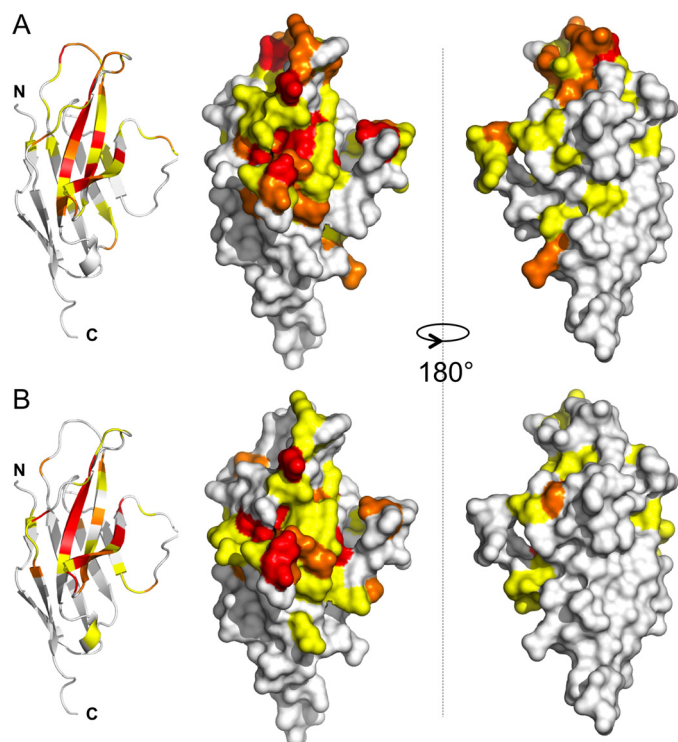


FIGURE 3. Regions of hPD-1 affected by PD-L1/PD-L2 binding. A, schematic and surface views of hPD-1 in which residues are colored according to the perturbation of their backbone (^{15}N , ^{13}C , and $^1\text{H}^{\text{N}}$) signals induced by hPD-L1 binding. Residues highlighted in B indicate the areas in hPD-1 affected by hPD-L2 binding. The color scheme used is relative for each complex (residues with minimal shift values lower than the S.D. value for the whole set are represented in white, residues with minimal shift values of $>1 \times \text{S.D.}$ are shown in yellow, residues with minimal shift values of $>1.5 \times \text{S.D.}$ are shown in orange, and residues with minimal shift values of $>2 \times \text{S.D.}$ are in red). Two views rotated by 180° are shown.

imposes a twist in the FG loop of hPD-1, allowing orthodox positioning of the BC loop, whereas in mPD-1 the BC loop is drawn toward the DE loop by a hydrophobic interaction involv-

ing Arg⁸³ (DE loop) and Trp³⁹ (BC loop). The second and most important region of difference is at the edge of the GFCC'/GFCC'C'' sheets where, for hPD-1, strand C'' is completely absent. Overall, the extracellular regions of human and mouse PD-1 are relatively highly conserved ($\sim 65\%$). The region of the C'D loop is among the least conserved parts of the sequence ($<50\%$; Fig. 1F), but the key difference is the substitution of Cys for Pro at position 63 of hPD-1, which shortens the C' strand by one residue and redirects the next eight residues away from strand C', producing a highly flexible loop (Fig. 1A).

Structural Basis of PD-L1 and PD-L2 Recognition

hPD-1·ligand complex formation was followed via perturbations of hPD-1 backbone NMR signals (^{15}N , ^{13}C , and $^1\text{H}^{\text{N}}$) induced by the ligands, hPD-L1 and hPD-L2 (Figs. 2 and 3). The changes were highly localized to a patch of residues on one face of hPD-1, with apparently no evidence of conformational changes being induced beyond this region. The addition of hPD-L1 significantly alters the positions of backbone signals for hPD-1 GFCC' β sheet residues centered on Gln⁵⁵ but also including Phe⁴³, Asn⁴⁶, Tyr⁴⁸, and Arg⁴⁹ (β -strand C); Ser⁵³ (CC' loop); Thr⁵⁶ and Ala⁶⁰ (strand C'); Asp⁶⁵ and Gln⁶⁸ (C'D loop); Arg⁹² (strand E); Thr¹⁰⁰, Leu¹⁰², Cys¹⁰³, Gly¹⁰⁴, and Ala¹⁰⁵ (strand F); Ala¹¹² and Gln¹¹³ (FG loop); Ser¹¹⁷ (strand G); Thr³⁹, Ser⁴⁰, and Glu⁴¹ (BC loop); and Leu¹⁰⁸ and Lys¹¹¹ (FG loop; Fig. 3A). These residues presumably form part of an interaction surface, first identified in crystals of mPD-1 and hPD-L1 (24). Similar but not identical shifts appeared in the presence of hPD-L2, involving a subset of the Gln⁵⁵-centered residues perturbed by hPD-L1 (*i.e.* Phe⁴³, Asn⁴⁶, Ser⁵³, Thr⁵⁶, Ala⁶⁰, Gln⁶⁸, Leu¹⁰², Cys¹⁰³, Gly¹⁰⁴, Ala¹⁰⁵, Gln¹¹³, and Ser¹¹⁷), but also including Met⁵⁰, Ser⁵¹, Asp⁵⁷, Leu⁵⁹, Phe⁶², Ser⁷³, Phe⁸⁶, and Ala¹²⁰ of the GFCC' β sheet and Ser³⁷ of the BC loop (Figs. 2B and 3B). Thus, the hPD-L2 binding surface is centered on Gln⁵⁵ of hPD-1 but with apparently smaller contributions from the

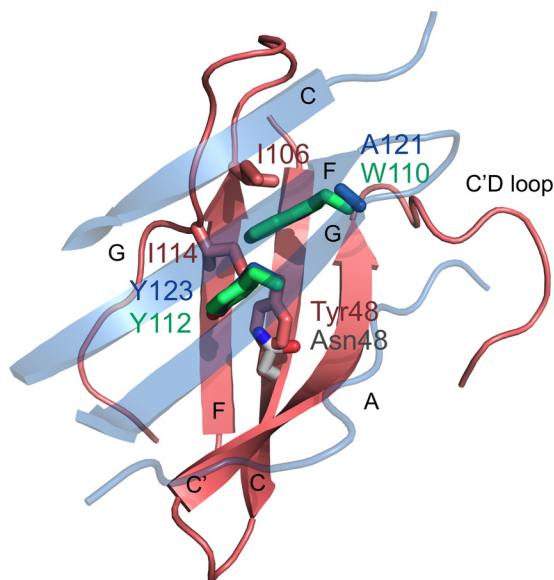


FIGURE 4. Portions of modeled or actual complexes of hPD-1 (red) and mPD-1 (gray), complexed with hPD-L1 (blue) and mPD-L2 (green). Only the GFCC' strands and extended C'D loop of hPD-1 and the AGFC strands of hPD-L1 are shown. hPD-1 (red), mPD-1 (gray), hPD-L1 (blue), and mPD-L2 (green) residues for which the model or actual complexes appear to be inconsistent with the levels of perturbation of the hPD-1 backbone signals in the presence of the ligands are shown in stick format (see "Results" for details).

hPD-1 BC and FG loops than for hPD-L1 binding. Overall, 22 of the 33 residues perturbed by either ligand in hPD-1 are conserved in mPD-1.

Models of the Complexes

To help interpret these apparent differences in binding modes, models of hPD-1·hPD-L1 and hPD-1·mPD-L2 complexes were built by superimposing hPD-1 onto the solved mPD-1·hPD-L1 (PDB code 3BIK) and mPD-1·mPD-L2 (PDB code 3BP5) structures (24, 25). hPD-1 surfaces buried in the models exhibit close overlap with those perturbed in the NMR analysis of binding, as expected given the high degree of conservation of the GFCC' sheet of PD-1 (data not shown) (53). However, there also appear to be significant discrepancies. First, in the modeled complexes, Tyr⁴⁸ at the center of the binding region of hPD-1 (Asn in mPD-1) interacts with a tyrosine (Tyr¹²³ in hPD-L1, Tyr¹¹² in mPD-L2) conserved in the ligands of both species (Fig. 4), but this residue is perturbed only by hPD-L1 in the NMR analysis. The substitution of Tyr⁴⁸ for Asn might otherwise have at least partly accounted for the weaker binding of the mouse proteins. Second, the C' strand of hPD-1 is perturbed in the presence of both hPD-L1 and hPD-L2 but not contacted by either ligand in the modeled complexes. Flexibility or a conformational change in the C'-D loop of hPD-1 might account for this difference. Third, in the modeled hPD-1·mPD-L2 complex a conserved tryptophan (Trp¹¹⁰) in strand G (Ala in PD-L1) is well positioned to contact Ile¹⁰⁶ and Ile¹¹⁴ of hPD-1 (Fig. 4), but neither Ile¹⁰⁶ nor Ile¹¹⁴ are perturbed by the ligands. However, the minimal shift values for these residues might have been underestimated due to spectral overlap with signals from other residues. This contact would account for the stronger binding of hPD-1 to hPD-L2 *versus* hPD-L1 (discussed below). Mutation of Ile¹⁰⁶ to Ala reduces

ligand binding by 70–80%, and mutation of Ile¹¹⁴ to Ala completely abrogates it (53). mPD-L2 undergoes slight conformational rearrangements in the region of the start of the C' strand and the BC loop when it binds mPD-1, whereas hPD-L1 binding is more "rigid body" in character (discussed in Ref. 25). These changes may be larger in hPD-L2 where the BC loop is not stabilized by disulfide bonding to the F strand (Cys⁴⁹–Cys¹⁰⁶). hPD-L2 binding may thus have substantial "induced fit" character, explaining its high affinity for PD-1 and the high enthalpy of the interaction (discussed below).

Biophysical Basis of Ligand Binding

Protein Expression—Large amounts of soluble, histidine-tagged forms of human and mouse hPD-L1 and hPD-L2 were produced in CHO cells, using approaches described previously (27–29). Biotinylated forms of the proteins were also expressed transiently in HEK 293T cells, as also described previously (46). In reducing and non-reducing SDS-polyacrylamide gels, the proteins migrated as broad bands of 45–60 kDa, consistent with heavy glycosylation; on gel filtration, the proteins eluted at the positions expected for monomers, which was taken to indicate that they were correctly folded (data not shown). Human and mouse PD-1 were expressed stably in the form of thrombin-cleavable chimeras with human IgG Fc (designated PD-1Fc) and released with thrombin prior to use as analytes (47). Soluble forms of human and mouse B7-1 were prepared as described previously (29) (all construct details are shown in supplemental Table S1).

Affinity and Kinetic Measurements—PD-1/ligand interactions were characterized using SPR-based assays at 37 °C. For equilibrium analysis of affinity, increasing amounts of hPD-1 were injected over immobilized biotinylated hPD-L1, hPD-L2, and sCD4 (used as a negative control). Binding reached equilibrium rapidly (>95% binding within 1–3 s), and during the wash phase, the base-line signal recovered quickly (within 5–15 s), reflecting very fast kinetics. Representative sensorgrams are shown in Fig. 5, A and C. Plots of specific binding *versus* concentration indicated that binding was saturable (Fig. 5, B and D). The good fit of the data to 1:1 Langmuir binding isotherms (Fig. 5, B and D) and the linear Scatchard plots (Fig. 5, B and D, insets) were consistent with a simple 1:1 Langmuir binding model. K_d values of $8.2 \pm 0.1 \mu\text{M}$ (mean \pm S.D., $n = 2$) and $2.3 \pm 0.1 \mu\text{M}$ ($n = 2$), respectively, were obtained for the binding of hPD-1 to hPD-L1 and hPD-L2 (Table 2). Measurements of these affinities in the opposite orientation (*i.e.* with hPD-1 immobilized and the ligands used as analytes) were in good agreement (Fig. 6 and Table 2). The binding of hB7-1 to hPD-L1 ($K_d \sim 18.8 \pm 3.8 \mu\text{M}$ ($n = 6$); Fig. 5, E and F) was substantially weaker than reported previously ($\sim 1.7 \mu\text{M}$) (23) for hB7-1 injected over immobilized hPD-L1. In the opposite orientation, a slightly higher K_d of $35.4 \pm 4.4 \mu\text{M}$ was obtained (Table 2). Kinetic analysis revealed that all affinity differences were almost entirely attributable to off-rate variation (Fig. 7 and Table 2).

The murine interactions were considerably weaker than the analogous human interactions. Moreover, the mPD-1/ligand affinities were the same, within error (K_d 29.8 ± 6.8 ($n = 8$) and $38.4 \pm 7.1 \mu\text{M}$ ($n = 8$) for mPD-1 binding to mPD-L1 and

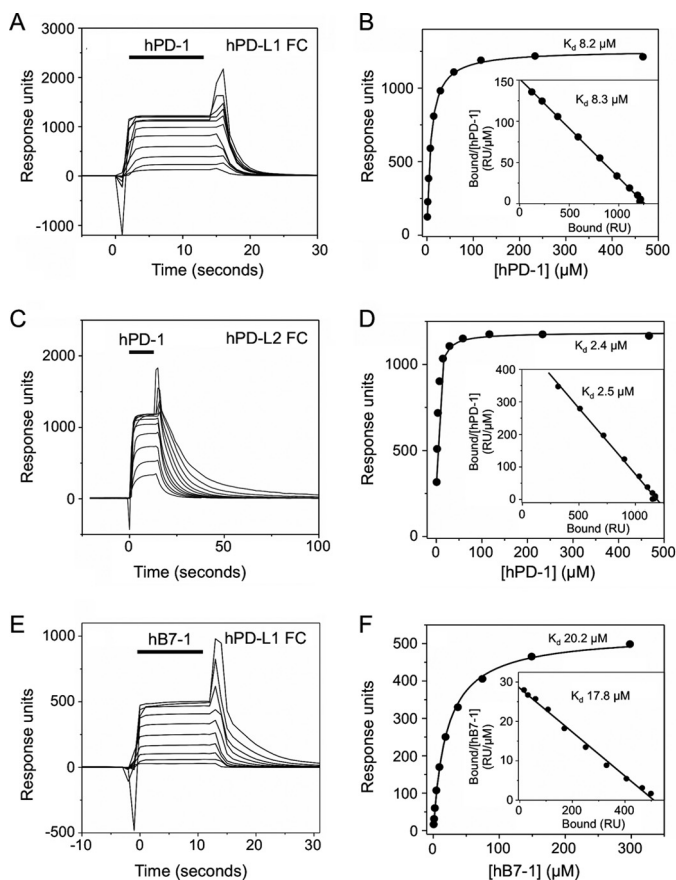


FIGURE 5. Human PD-1/PD-1 ligand and hPD-L1/B7-1 interactions (equilibrium binding analyses). *A*, hPD-1, at a range of concentrations (930 μM and 2-fold dilutions thereof), was injected at 20 $\mu\text{l}/\text{min}$ sequentially (solid bar) through a flow cell containing ~ 2000 RU of indirectly immobilized hPD-L1 at 37 $^{\circ}\text{C}$. Background responses observed in a control flow cell containing immobilized hCD4 were subtracted from the total responses to give binding. *B*, nonlinear curve fitting of the untransformed data using a 1:1 Langmuir binding isotherm yielded a K_d of 8.2 μM and a binding maximum of 1257 RU. A linear Scatchard plot of the hPD-1/hPD-L1 binding data (inset) yielded a similar K_d of 8.3 μM . *C*, hPD-1, at a range of concentrations (930 μM and 2-fold dilutions thereof), was injected as in *A* through a flow cell containing ~ 2000 RU of indirectly immobilized hPD-L2 at 37 $^{\circ}\text{C}$. Background responses have been subtracted. *D*, nonlinear curve fitting of the untransformed data using a 1:1 Langmuir binding isotherm yielded a K_d of 2.4 μM and a binding maximum of 1185 RU. A linear Scatchard plot of the hPD-1/hPD-L2 binding data (inset) yielded a similar K_d of 2.5 μM . *E*, hB7-1, at a range of concentrations (596 μM and 2-fold dilutions thereof), was injected as in *A* through a flow cell containing ~ 2000 RU of indirectly immobilized hPD-L1 at 37 $^{\circ}\text{C}$. Background responses have been subtracted. *F*, nonlinear curve fitting of the untransformed data using a 1:1 Langmuir binding isotherm yielded a K_d of 20.2 μM and a binding maximum of 525 RU. A linear Scatchard plot of the hB7-1/hPD-L1 binding data (inset) yielded a similar K_d of 17.8 μM .

mPD-L2, respectively), in marked contrast to the interactions of hPD-1 (Fig. 8, *A–D*). The affinity of mB7-1 for mPD-L1 was very low, at $80.3 \pm 6.8 \mu\text{M}$ ($n = 6$; Fig. 8, *E* and *F*, and Table 2).

Thermodynamic Measurements—For thermodynamic analysis, the soluble forms of PD-L1 and PD-L2 were mixed with hPD-1 in the form of uncleaved Fc fusion protein. Representative data for the isothermal calorimetric titration of the hPD-1Fc dimer with hPD-L1 and hPD-L2 at 25 $^{\circ}\text{C}$ are shown in Fig. 9, *A* and *B*; titrations performed at other temperatures gave similar quality data (Table 3) (data not shown). The heats of interaction were not very large, but isotherms could be readily fitted to the data. The binding stoichiometry for both ligands is 1:1, in accordance with the finding that human PD-1 is mono-

meric in solution and at the cell surface (53). At the temperatures investigated (10–25 $^{\circ}\text{C}$), the affinity of hPD-L2 for hPD-1Fc was ~ 5 –8-fold higher than that of hPD-L1 for hPD-1Fc, in good agreement with the ratio obtained by SPR analysis (Tables 2 and 3). However, the SPR-derived affinities were somewhat lower than those measured by ITC, as observed elsewhere (21).

Thermodynamic parameterization (Table 3) reveals that the hPD-1/ligand interactions are subtly different. Under all conditions, both interactions have favorable ΔH_{obs} and $T\Delta S$, but hPD-1/hPD-L1 binding is entropically driven, whereas the hPD-1/hPD-L2 interaction has a large enthalpic term. The binding differences do not seem to be based on charge or protonation effects because the data are largely invariant at the different pH values and salt concentrations. The differences are not manifested in the temperature dependence of the thermodynamic parameters either. ΔH_{obs} for the association of hPD-1 with hPD-L1 and hPD-L2 declines linearly from +0.8 kcal mol $^{-1}$ at 15 $^{\circ}\text{C}$ to -2.77 kcal mol $^{-1}$ at 25 $^{\circ}\text{C}$ and from -4.6 kcal mol $^{-1}$ to -7.7 kcal mol $^{-1}$, respectively (Fig. 9C), yielding very similar ΔC_p terms of -233 and -205 cal mol $^{-1}$ K $^{-1}$, respectively. Because ΔC_p is usually dominated by solvent effects, it implies that the hydrophobic surface areas buried in forming the two complexes are very similar. Overall, the interaction of hPD-1 with its ligands is robust with respect to possible fluctuations in extracellular conditions. The lack of effects of temperature, pH, and salt conditions suggests that the differences in affinity and thermodynamic parameters are most likely the result of minor changes in the formation of non-covalent interactions in the binding sites.

Simulations of PD-1/Ligand and PD-L1/B7-1 Interactions

Molecule Expression Levels—In order to simulate complex formation by human PD-1 at cellular synapses, we obtained quantitative expression data for each of the proteins using flow cytometry. Resting and phytohemagglutinin-activated CD3 $^{+}$ human T cells were stained with phycoerythrin (PE)-conjugated anti-PD-1, anti-PD-L1, anti-PD-L2, and anti-B7-1 antibodies alongside beads conjugated with known different amounts of PE. hPD-1 and hPD-L1 were undetectable on resting T cells. Following activation, however, these proteins reached expression levels of $\sim 3000/\text{cell}$ and $\sim 9000/\text{cell}$, respectively, consistent with previous findings (54, 55) (Fig. 10A). B7-1 was undetectable under either condition, however. PD-L1 and PD-L2 were expressed by *in vitro* prepared (50) immature and mature human DCs at levels of ~ 5000 and ~ 700 copies/cell (immature DCs) and $\sim 80,000$ and ~ 5000 copies/cell (mature DCs), respectively (Fig. 10B). The numbers of CD28, CTLA-4, B7-1, and B7-2 molecules used in the simulations were based on previous estimates (50).

Simulations—Complex formation was simulated using a system of nonlinear ordinary differential equations, incorporating the stoichiometric, affinity, and expression data, as described previously (Table 4) (50) (see supplemental Experimental Procedures for details). Briefly, the three-dimensional k_{on} values were converted to two-dimensional on-rates using the methods of Bell (56). Simulations begin at the time an activated T cell forms a synapse with a mature DC because human PD-1 and PD-L1 were undetectable on naive cells. The cell surfaces are

Structure and Interactions of PD-1

TABLE 2

Affinity and kinetic parameters for PD-1 binding to PD-L1 and PD-L2

Interactions of human and mouse PD-1 with PD-L1 or PD-L2 were characterized at 37 °C using SPR-based assays as implemented by Biacore™.

	Interaction								
	hPD-1/hPD-L1		hPD-1/hPD-L2		hPD-L1/hB7-1		mPD-1/mPD-L1	mPD-1/mPD-L2	mPD-L1/mB7-1
Analyte	hPD-1	hPD-L1	hPD-1	hPD-L2	hPD-L1	hB7-1	mPD-1	mPD-1	mB7-1
<i>n</i>	2	6	2	6	4	6	8	8	6
K_d (μM) ^a	8.2 ± 0.1	7.5 ± 2.2	2.3 ± 0.1	2.2 ± 0.2	35.4 ± 4.4	18.8 ± 3.8	29.8 ± 6.8	38.4 ± 7.1	79.3 ± 3.6
k_{on}^b ($\text{M}^{-1} \text{s}^{-1}$)	1.84 × 10 ⁵		2.5 × 10 ⁵		3.16 × 10 ⁵		ND ^c	ND	ND
k_{off}^d (s^{-1})	1.44 ± 0.21		0.55 ± 0.05		5.94 ± 0.12		ND	ND	ND

^a Means and S.D. are shown; K_d values were obtained by non-linear fitting of 1:1 Langmuir binding isotherms.

^b Each k_{on} was calculated from the equation $k_{\text{on}} = k_{\text{off}}/K_d$.

^c ND, not determined.

^d k_{off} ($k_{\text{off}} = \text{mean} \pm \text{S.D.}$) was calculated via the fitting of global 1:1 binding models to the data.

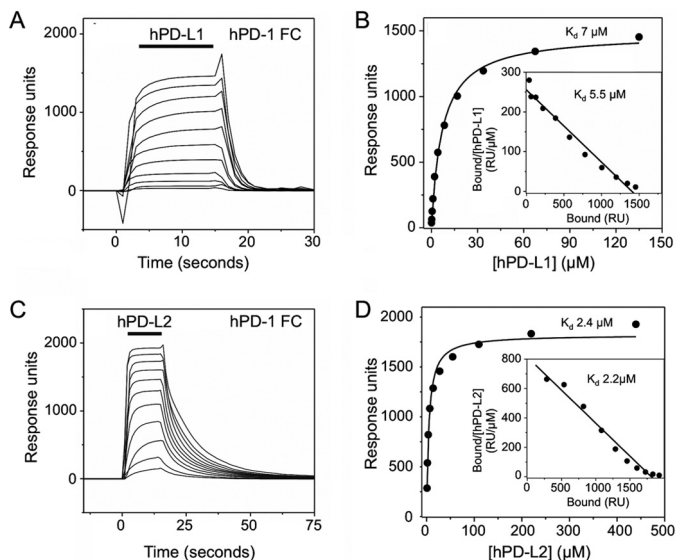


FIGURE 6. hPD-1/hPD-L1 equilibrium binding analyses (reverse orientation). A, hPD-L1, at a range of concentrations (135 μM and 2-fold dilutions thereof) was injected at 20 $\mu\text{l}/\text{min}$ sequentially (solid bar) through a flow cell containing ~ 4000 RU of directly immobilized hPD-1Fc at 37 °C. Background responses observed in a control flow cell containing immobilized hCD28Fc were subtracted from the total responses to give binding. B, nonlinear curve fitting of the untransformed data using a 1:1 Langmuir binding isotherm yielded a K_d of 7.0 μM and a binding maximum of 1480 RU. A linear Scatchard plot of the hPD-1/hPD-L1 binding data (inset) yielded a similar K_d of 5.5 μM . C, hPD-L2, at a range of concentrations (220 μM and 2-fold dilutions thereof), was injected as in A through a flow cell containing ~ 5000 RU of directly immobilized hPD-1Fc at 37 °C. Background responses have been subtracted. D, nonlinear curve fitting of the untransformed data using a 1:1 Langmuir binding isotherm yielded a K_d of 2.4 μM and a binding maximum of 1822 RU. A linear Scatchard plot of the hPD-1/hPD-L2 binding data (inset) yielded a similar K_d of 2.2 μM .

divided into the synapse (c-SMAC) and the region outside the synapse, and freely diffusing unbound mobile molecules are recruited to the synapse by ligation. In simulations of human PD-1/ligand interactions as a function of time (Fig. 10C), human PD-1 accumulation in the synapse reaches a steady state within 15 min. Although human PD-1 binds PD-L2 with a ~ 3.5 -fold higher affinity than it binds PD-L1, it forms 5-fold fewer PD-1·PD-L2 than PD-1·PD-L1 complexes at steady state due to the 15-fold lower expression of PD-L2 versus PD-L1. Varying the expression level of PD-L2 reveals that the human PD-1/PD-L1 interaction is only sensitive to increasing PD-L2 levels at very high levels of PD-L2 ($> 5 \times 10^4$; Fig. 10D). Conversely, human PD-1 engagement by PD-L2 is largely insensitive to PD-L1 at all levels of PD-L1 expression (Fig. 10E). The relatively low level of human PD-1 engagement by PD-L2 is

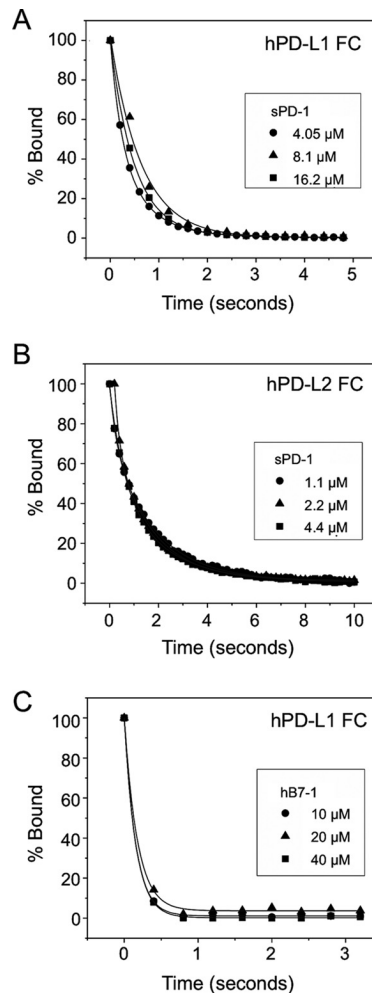


FIGURE 7. Kinetic analyses. A, hPD-1, at concentrations of 4.05, 8.1, and 16.2 μM , was injected at 100 $\mu\text{l}/\text{min}$ at 37 °C over ~ 250 RU of indirectly immobilized hPD-L1 and allowed to dissociate at the end of each injection. Data were recorded at the maximal collection rate (10 Hz) until the response had returned to base line. Responses in a control flow cell were subtracted, and the remaining binding was plotted as a percentage of initial binding. The data are fitted with single exponential decay curves, giving a k_{off} value of $1.97 \pm 0.19 \text{ s}^{-1}$ (mean \pm S.D., $n = 9$). B, dissociation of hPD-1 from hPD-L2 at 37 °C. hPD-1 (1.1, 2.2, and 4.4 μM) was injected over ~ 100 RU of indirectly immobilized hPD-L2 at 100 $\mu\text{l}/\text{min}$. The data are fitted with single exponential decay curves, giving a k_{off} value of $0.71 \pm 0.07 \text{ s}^{-1}$ (mean \pm S.D., $n = 9$). C, dissociation of hB7-1 from hPD-L1 at 37 °C. hB7-1 (10, 20, and 40 μM) was injected over ~ 350 RU of indirectly immobilized hPD-L1 at 100 $\mu\text{l}/\text{min}$. The data are fitted with single exponential decay curves, giving a k_{off} value of $6.44 \pm 0.38 \text{ s}^{-1}$ (mean \pm S.D., $n = 9$).

therefore not due to competition with PD-L1 at physiological expression levels. Simulations incorporating the K_d values for the murine interactions (Table 2), using the human expression

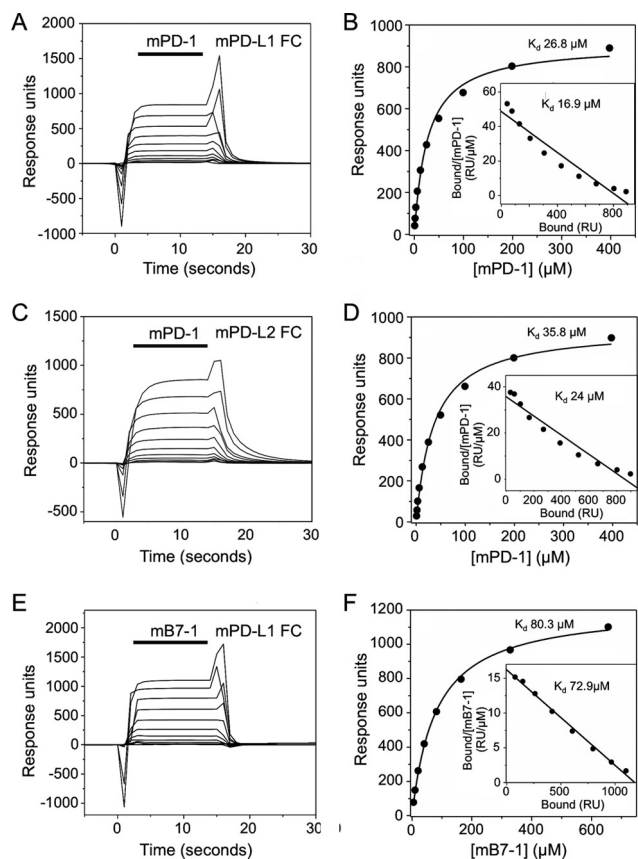


FIGURE 8. Murine PD-1/PD-L1 interactions (equilibrium binding analyses). *A*, mPD-1, at a range of concentrations (398 μM and 2-fold dilutions thereof) was injected at 20 $\mu\text{l}/\text{min}$ sequentially (*solid bar*) through a flow cell containing ~ 2000 RU of indirectly immobilized mPD-L1 at 37 $^{\circ}\text{C}$. Background responses observed in a control flow cell containing immobilized hCD4 were subtracted from the total responses to give binding. *B*, nonlinear curve fitting of the untransformed data using a 1:1 Langmuir binding isotherm yielded a K_d of 26.8 μM and a binding maximum of 908 RU. A Scatchard plot of the mPD-1/mPD-L1 binding data (*inset*) yielded a K_d of 16.9 μM . *C*, mPD-1, at a range of concentrations (398 μM and 2-fold dilutions thereof) was injected as in *A* through a flow cell containing ~ 2000 RU of indirectly immobilized mPD-L2 at 37 $^{\circ}\text{C}$. Background responses have been subtracted. *D*, nonlinear curve fitting of the untransformed data using a 1:1 Langmuir binding isotherm yielded a K_d of 35.8 μM and a binding maximum of 946 RU. A Scatchard plot of the mPD-1/mPD-L2 binding data (*inset*) yielded a K_d of 24 μM . *E*, mB7-1, at a range of concentrations (655 μM and 2-fold dilutions thereof) was injected as in *A* through a flow cell containing ~ 2000 RU of indirectly immobilized mPD-L1 at 37 $^{\circ}\text{C}$. Background responses have been subtracted. *F*, nonlinear curve fitting of the untransformed data using a 1:1 Langmuir binding isotherm yielded a K_d of 80.3 μM and a binding maximum of 1215 RU. A Scatchard plot of the mB7-1/mPD-L1 binding data (*inset*) yielded a similar K_d of 72.9 μM .

data, result in ~ 3 -fold and ~ 20 -fold reductions in mouse PD-1 \cdot PD-L1 and PD-1 \cdot PD-L2 complex formation, respectively (Fig. 11A), due to the weaker affinities.

Although we were unable to detect B7-1 expression on activated T cells, others have (57–59). To explore the likelihood that B7-1 expression on T cells affects PD-1 engagement, we estimated the steady state levels of bound PD-1 and B7-1 molecules as a function of varying B7-1 expression. B7-1 only began to affect PD-1 \cdot PD-L1 complex formation when expressed at >5000 molecules/cell (Fig. 10F). It therefore seems unlikely that B7-1 would have any appreciable effect on PD-1 ligation because even mature DCs do not express more than 4000 B7-1 molecules/cell (50).

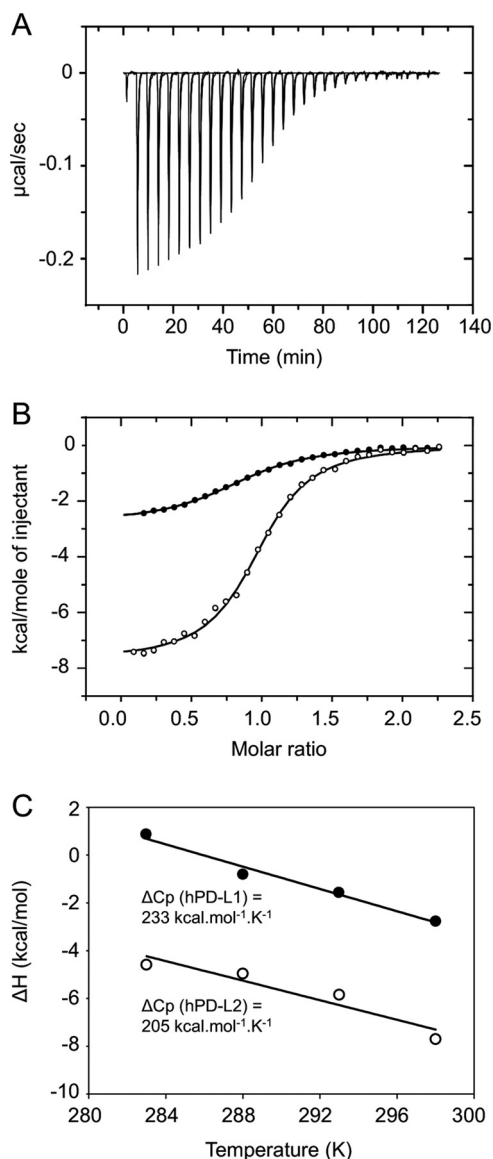


FIGURE 9. ITC measurements of hPD-1 binding to PD-L1 and PD-L2. *A*, example of raw data for titration of hPD-L2 at 0.2 mM into an isothermal calorimetry cell containing a 0.02 mM solution of hPD-1Fc at pH 7.4 and 25 $^{\circ}\text{C}$ in a buffer containing 150 mM NaCl. Similar titrations were undertaken at various temperatures, the results of which are summarized in Table 3. *B*, plots of heat-released versus molar ratio for the interactions of hPD-L1 (*closed circles*) and hPD-L2 (*open circles*) with hPD-1. *C*, plots of observed enthalpy versus temperature for the interactions of hPD-L1 (*closed circles*) and hPD-L2 (*open circles*) with hPD-1. The slopes of these plots give the change in heat capacity (ΔC_p) upon binding of hPD-L1 and hPD-L2 to hPD-1, the values of which are -233 and -205 $\text{cal mol}^{-1} \text{K}^{-1}$, respectively.

The K_d values obtained in this study are 10–16-fold larger than those obtained previously (23). In simulations of B7-1/PD-L1 binding at the older, higher affinities, the numbers of bound PD-1 and B7-1 molecules at steady state increase in direct proportion to the respective affinity differences (data not shown). The implication is that the effects of PD-L1/B7-1 binding on the competing interactions of each of these proteins would have been significant if the previous measurements of these affinities were reliable. However, using the K_d values obtained in the present study for the B7-1 and PD-L1 interaction, the inclusion of PD-L1 in our previous model (50) barely affects the ligation of CD28 and CTLA-4 (Fig. 11B).

TABLE 3

Thermodynamic properties of hPD-1 binding to hPD-L1 and hPD-L2

Interactions of PD-1 with PD-L1 or PD-L2 were characterized at a range of temperatures from 10 to 25 °C by quantitative ITC analysis.

	Binding parameters					
	n^a	K $10^5 M^{-1}$	K_d^a μM	ΔH^a $kcal mol^{-1}$	$-T\Delta S^b$ $kcal mol^{-1}$	ΔG $kcal mol^{-1}$
hPD-1 binding to hPD-L1						
pH 6.0	0.904 ± 0.0098	6.28 ± 0.47	1.6	-2.23 ± 0.033	-5.66	-7.9
pH 7.4	0.865 ± 0.015	4.58 ± 0.49	2.2	-2.88 ± 0.068	-4.83	-7.7
pH 8.0	0.906 ± 0.018	3.29 ± 0.34	3.04	-2.69 ± 0.077	-4.83	-7.5
10 °C	1.23 ± 0.032	2.96 ± 0.65	3.38	0.87 ± 0.037	-7.95	-7.5
15 °C	0.602 ± 0.014	5.76 ± 1.80	1.74	-0.81 ± 0.078	-6.8	-7.8
20 °C	0.882 ± 0.014	5.11 ± 0.48	1.96	-1.56 ± 0.035	-6.09	-7.8
25 °C	0.878 ± 0.057	5.41 ± 0.21	1.85	-2.77 ± 0.026	-5.07	-7.8
50 mM NaCl	0.842 ± 0.0073	6.15 ± 0.34	1.63	-3.24 ± 0.038	-4.65	-7.9
500 mM NaCl	0.902 ± 0.017	5.15 ± 0.61	1.94	-2.21 ± 0.058	-5.57	-7.8
hPD-1 binding to hPD-L2						
pH 6.0	1.08 ± 0.0055	20.2 ± 0.97	0.5	-6.18 ± 0.043	-2.42	-8.6
pH 7.4	1.11 ± 0.0075	22.2 ± 1.50	0.45	-6.50 ± 0.059	-2.15	-8.66
pH 8.0	1.04 ± 0.006	17.8 ± 0.90	0.56	-7.24 ± 0.057	-1.29	-8.53
10 °C	0.982 ± 0.012	23.7 ± 2.60	0.42	-4.57 ± 0.081	-3.71	-8.5
15 °C	0.988 ± 0.015	37.7 ± 6.80	0.27	-4.96 ± 0.10	-3.72	-8.8
20 °C	1.09 ± 0.018	29.5 ± 5.50	0.34	-5.84 ± 0.14	-2.84	-8.7
25 °C	0.979 ± 0.0063	26.3 ± 1.70	0.38	-7.70 ± 0.067	-1.06	-8.8
50 mM NaCl	1.01 ± 0.0056	20.8 ± 1.10	0.48	-7.57 ± 0.057	-1.05	-8.6
500 mM NaCl	0.985 ± 0.0068	21.7 ± 1.40	0.46	-7.35 ± 0.068	-1.29	-8.6

^a The values for K_d , stoichiometry, and ΔH , obtained by fitting a single binding site model to the ITC data, are shown with S.E. values.^b The ΔS value was calculated using the equation, $\Delta G = -RT \times \ln(K_d) = \Delta H_{obs} - T\Delta S$.

DISCUSSION

PD-1 plays an important role in down-regulating immune responses, reportedly via a number of different mechanisms after binding its ligands PD-L1 and PD-L2. Previous studies revealed that PD-L1 and PD-L2 have similar structures but very different expression patterns and expression kinetics (15). The unexpected finding that PD-L1 also binds B7-1 further complicates matters (22, 23). A detailed understanding of the structures and interactions of PD-1 should aid in rationalizing this complexity.

Our NMR-derived structure of human PD-1 is most similar to antigen receptor domains, consistent with a shared evolutionary origin (21). Human PD-1 is, however, surprisingly different from its murine ortholog. Whereas mouse PD-1 has a "conventional" IgSF V-set domain, the human receptor lacks a C' strand, and instead the C' and D strands are connected by a relatively long and flexible loop. Moreover, the BC loop is not stabilized by disulfide bonding to the F strand of the ligand binding β sheet. These interspecies differences are apparently responsible for the surprising differences in the affinities of human and mouse PD-1 for their ligands (discussed below) because mouse PD-L1 and PD-L2 have the same affinities for hPD-1 as their human counterparts (data not shown). Although human PD-1 is relatively flexible, this does not present a large barrier to ligand binding because the overall binding entropies are favorable. Perturbations of hPD-1 backbone NMR signals in the presence of its ligands, combined with thermodynamic analysis of binding, revealed that the ligands bind in apparently different ways to the same site on hPD-1, with PD-L2 appearing to form a smaller interface with possibly better geometric complementarity than PD-L1, aided perhaps by local conformational rearrangements. Another explanation for the enthalpic nature of this interaction is that during hPD-1 and PD-L2 binding, an additional water molecule(s) is incorporated. This would have a negative ΔH effect due to additional hydrogen

bonding but at an entropic cost. The ΔC_p values for human PD-1/PD-L1 and PD-1/PD-L2 binding were very similar, consistent with the involvement of large hydrophobic areas ($\sim 1000 \text{ \AA}^2$) in the binding of both ligands. However, neither ligand bound human PD-1 in a way that was fully explained by the crystal structures of the mouse PD-1·ligand complexes, although the binding surface, defined by the ligand-induced perturbations of the human PD-1 backbone residues, is relatively highly conserved (*i.e.* 22 of 33 residues). Overall, the divergence of the human and mouse structures seems only to have been constrained by the need to retain the ligand-binding surface.

Perhaps the most striking finding of the present study is that the interactions of this inhibitory receptor are relatively weak and much weaker than those of the other key inhibitory protein expressed by T cells, CTLA-4. Interactions within the CD28/CTLA-4 system differ in strength due to affinity differences and stoichiometric effects; the affinities vary by ~ 2 orders of magnitude from the strongest (CTLA-4·B7-1) to the weakest (CD28·B7-2), with the bivalency of CTLA-4 and B7-1 further accentuating these differences (by ~ 2 more orders of magnitude (28)), such that the half-lives of inhibitory (CTLA-4·B7-1) and activating (CD28·B7-2) complexes may differ $>10,000$ -fold. For the human PD-1 system, such large differences are not possible; the affinities differ only 3–4-fold, and the proteins are all monovalent (53). Thus, the half-lives of human PD-1·PD-L1 ($K_d \sim 8 \mu M$) and PD-1·PD-L2 ($K_d \sim 2 \mu M$) signaling complexes will probably be 1000–5000-fold shorter than that of CTLA-4·B7-1 complexes. Murine PD-1·ligand complexes (30–35 μM) will probably be even shorter lived. The very stable CTLA-4·B7-1 complexes formed after T cell activation were thought to be required to turn off activating signals delivered by CD28 (28, 60). However, it now seems that very stable complexes are not a prerequisite for potent inhibitory signaling.

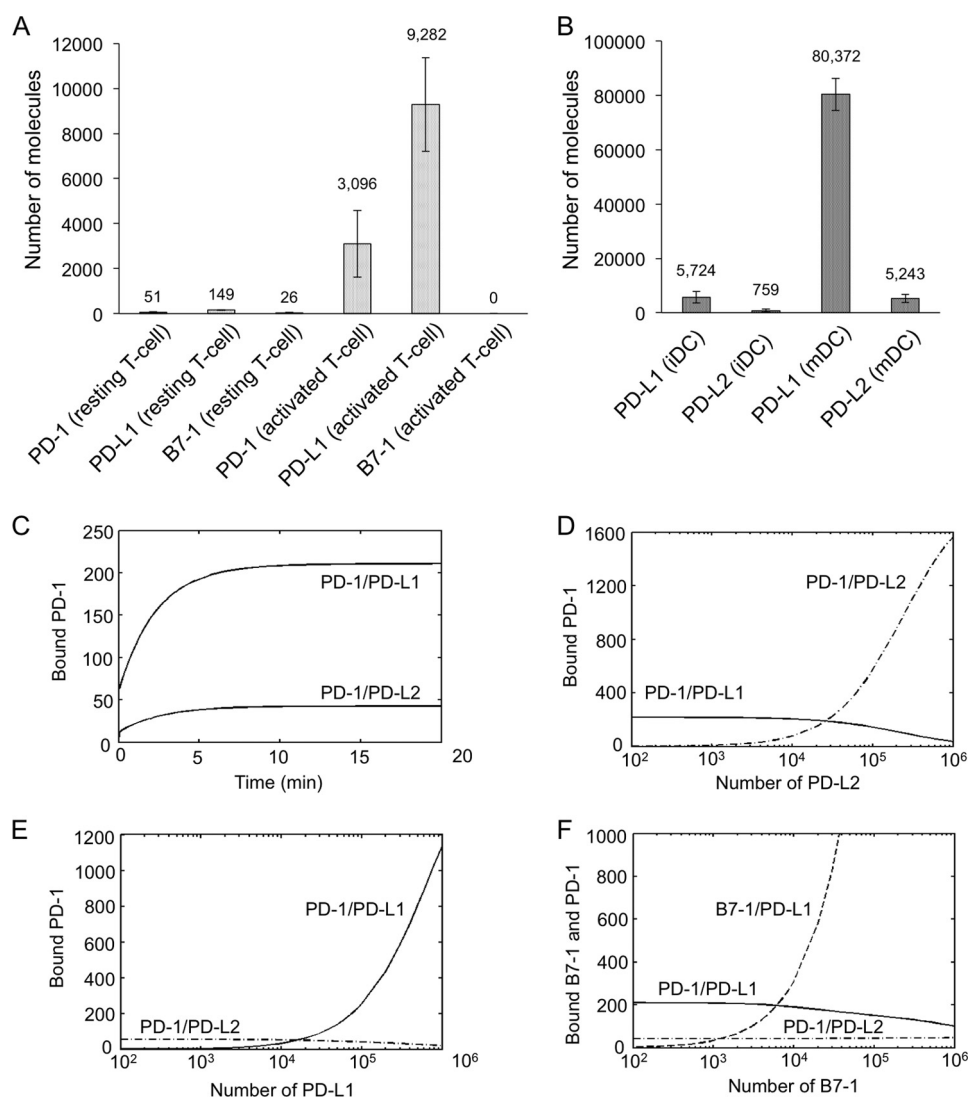


FIGURE 10. Simulations of human PD-1/ligand and PD-L1/B7-1 interactions based on affinity and expression data. *A*, the expression levels of human PD-1, PD-L1, and B7-1 on resting and activated human T cells. Peripheral blood mononuclear cells were activated with PHA (50 $\mu\text{g}/\text{ml}$) for 2 days. Cells were stained with PE-conjugated mAbs for each protein and analyzed by flow cytometry. QuantiBRITE PE beads were analyzed alongside the stained peripheral blood mononuclear cell samples. The experiments were done in duplicate. The average of two sets of data is shown; the *error bars* indicate S.D. *B*, expression levels for PD-L1 and PD-L2 on immature DCs and mature DCs. DCs were derived by using GM-CSF (50 ng/ml) and IL-4 (50 ng/ml) for 6 days. CD14⁺ monocytes were initially isolated from human peripheral blood mononuclear cells using CD14 MACs beads (Miltenyi Biotec). Immature DCs were then stimulated with LPS (1 $\mu\text{g}/\text{ml}$) for 24 h to obtain mature DCs. Cells were stained with PE-conjugated mAbs for each protein and analyzed by flow cytometry. The experiments were done in duplicate. The average of two sets of data are shown; *error bars* indicate S.D. *C–F*, simulations of molecular complex formation at the synaptic interface between an activated T cell and a mature DC. *C*, numbers of bound PD-1 molecules over time. *D* and *E*, number of bound PD-1 molecules at steady state as a function of varying the number of PD-L2 or PD-L1 molecules on the DC. *F*, number of bound PD-1 and B7-1 molecules at steady state as a function of varying the number of B7-1 molecules on the T cell.

PD-1 engagement is more effective than CTLA-4 ligation in suppressing gene transcription induced by CD3/CD28-generated signals (61), also suggesting that PD-1 and CTLA-4 block T cell activation in different ways, given that PD-1 also relies on much weaker interactions. PD-1 and CTLA-4 both block Akt activation, albeit using distinct mechanisms (61); PD-1 inhibits Akt by blocking PI3K activation, whereas CTLA-4 uses PP2A to inhibit Akt. CTLA-4 engagement also disrupts the recruitment of ZAP70 to microclusters, reversing the “stop” signal induced by TCR signaling, thereby inhibiting activation (62). PD-1 is also proposed to disrupt the stop signal via the recruitment of the SHP-2 phosphatase to microclusters (14). But it is possible that CTLA-4 is not a conventional signaling receptor. Consistent with its formidable binding properties, it is suggested that CTLA-4 exerts its inhibi-

tory effect on CD28 signaling by depleting their mutual ligands B7-1 and B7-2 from apposing cells via *trans*-endocytosis (63). The very much weaker interactions of PD-1 probably make it incapable of such effects, which would in any case only limit its inhibitory potential because it does not share ligands with activating receptors, unlike CTLA-4. The cytoplasmic domains of CTLA-4 and CD28 bind to a remarkably similar spectrum of Src homology 2 domains, suggesting that at the signaling level, CTLA-4 might not be any more inhibitory than CD28. PD-1, however, binds an entirely different set of Src homology 2 domains, including SHP-2, as expected for an inhibitory as opposed to an activating receptor.⁵

⁵ J. H. and S. J. D., unpublished data.

Structure and Interactions of PD-1

TABLE 4
Parameter values used for the computational simulations

Name	Definition	Value	Reference/Source
$a_{T_{cell}}$	Area of an activated T cell	$452 \mu\text{m}^2$	Ref. 1
a_{DC}	Area of a dendritic cell	$1256 \mu\text{m}^2$	Ref. 1
a_{syn}	Area of synapse (c-SMAC)	$12.6 \mu\text{m}^2$	Ref. 1
γ_{DC}	Rate constant for molecules on DC diffusing into synapse	$2.7 \times 10^{-4} \text{s}^{-1}$	Ref. 1
κ_{DC}	Rate constant for molecules on DC diffusing out from synapse	$2.7 \times 10^{-2} \text{s}^{-1}$	Ref. 1
γ_T	Rate constant for molecules on T cells diffusing into synapse	$1.0 \times 10^{-3} \text{s}^{-1}$	Ref. 1
κ_T	Rate constant for molecules on T cells diffusing out from synapse	$3.6 \times 10^{-2} \text{s}^{-1}$	Ref. 1
m	Fraction of mobile cell surface molecules	0.6^a	Ref. 3
α_1	Association of PD-1 and PD-L1	$0.10 \mu\text{m}^2 \text{s}^{-1}$	This work
α_2	Association of PD-1 and PD-L2	$0.14 \mu\text{m}^2 \text{s}^{-1}$	This work
α_3	Association of B7-1 and PD-L1	$0.17 \mu\text{m}^2 \text{s}^{-1}$	This work
α_4	Association of B7-1 monomers	$0.03 \mu\text{m}^2 \text{s}^{-1}$	Ref. 4
α_{33}	Bivalent association of B7-1 and PD-L1	$0.17 \mu\text{m}^2 \text{s}^{-1}$	This work
δ_1	Dissociation of PD1·PDL1 complexes	1.44s^{-1}	This work
δ_2	Dissociation of PD1·PDL2 complexes	0.55s^{-1}	This work
δ_3	Dissociation of B71·PDL1 complexes	5.94s^{-1}	This work
δ_4	Dissociation of B7-1 dimer	1s^{-1}	Ref. 4
δ_{33}	Dissociation of bivalent B7-1·PD-L1 complexes	5.94s^{-1}	This work

^a The motilities of the cell surface molecules were assumed to be the same as the ones observed for CD2 (50).

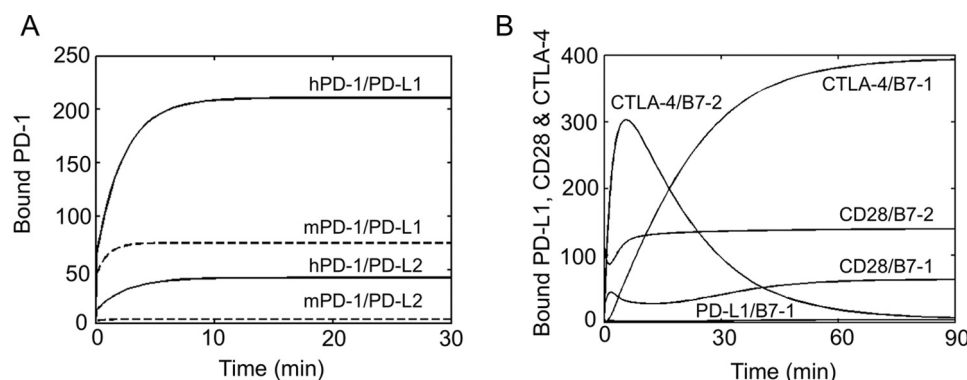


FIGURE 11. Simulations of murine PD-1/ligand interactions and effects of PD-L1/B7-1 interactions on CD28 and CTLA-4 ligation. A, number of bound PD-1 molecules over time. The simulations are based on human K_d values (solid lines) and on mouse K_d values (dashed lines) obtained in the present study. The expression values and off-rates obtained for human PD-1 and its ligands are used in both simulations because the corresponding mouse data are not available. B, number of bound PD-L1, CD28, and CTLA-4 as a function of time. The effect of PD-L1 on the CD28 and CTLA-4 ligation to their B7 ligands was simulated by incorporating the interaction between PD-L1 and B7-1 in our previous model of the costimulatory system (50). Because PD-L1 only binds to a few B7-1 molecules, PD-L1 expression barely affects CD28 and CTLA-4 ligation.

It might be that, in general, the binding affinities of conventional inhibitory receptors are not substantially different from those of activating receptors.

Once formed, human PD-1·PD-L2 complexes will probably be ~3-fold more stable than PD-1·PD-L1 complexes. This could lead to differential phosphorylation of the tyrosine residues in the cytoplasmic ITIM and ITSM motifs of PD-1, resulting in qualitatively different signals in response to each of the ligands. Because the expression of PD-L2 is thought to be largely restricted to “professional” antigen-presenting cells (15), it might be important for these cells to generate distinct signals. However, there now appear to be two problems with this argument. First, our simulations of the interactions of activated T cells and mature DCs suggest that human PD-1 will engage ~4-fold more PD-L1 than PD-L2 molecules due to the low expression of PD-L2 on mature DCs, despite the 3–4-fold lower affinity of PD-L1. Only when the expression of PD-L2 is increased ~4-fold is the level of accumulation of PD-1·PD-L2 complexes comparable with that of PD-1·PD-L1 complexes. This suggests that signaling at contacts with mature DCs could be dominated by PD-L1. The second issue is that the ~4-fold higher affinity of human PD-L2 *versus* PD-L1 is not observed in mice, arguing against affinity differences being highly signifi-

cant (the affinity of the PD-1/PD-L1 interaction is in fact slightly higher in mice: $K_d \sim 29.8 \mu\text{M}$ *versus* $\sim 38.4 \mu\text{M}$). One theoretical possibility is that the binding of PD-L1 and PD-L2 induces different conformational rearrangements in PD-1, resulting in distinct types of signals. However, the localized and largely similar effects of the ligands on PD-1 backbone NMR signals, which we found to be restricted to one face only, appear to rule this out (for human PD-1 at least). Overall, the intrinsic signaling properties of PD-L1 and PD-L2 in the mouse seem likely to be identical, suggesting that a capacity to produce differential signals is not the *raison d'être* of the paired ligands. However, it is also clear that PD-L1 and PD-L2 are not functionally redundant, even in mice. In PD-L1-deficient mice, CD8⁺ T cells spontaneously accumulate in the liver, accelerating hepatocyte damage in an experimental model of autoimmune hepatitis (64), whereas antigen-specific CD8⁺ T cell responses and cytotoxic T lymphocyte activity are diminished in PD-L2-deficient mice (65). At present, these effects cannot be explained by the known biophysical properties of these interactions. It must, however, be acknowledged that we might have failed to mimic the actual patterns of *in vivo* expression of PD-L1/2 in our simulations.

A final matter concerns the likely impact of B7-1/PD-L1 interactions on PD-1, CD28, and CTLA-4 function. The affinity data used to support a competition model (22) were obtained with the use of bivalent forms of the proteins, which it now seems greatly overestimated the strength of the B7-1/PD-L1 interaction. There is little chance of B7-1 and PD-L1 being present at interfaces without other binding competitors, but the affinity of their interaction according to the present study is at least 2-fold and as much as ~100-fold lower than that of other interactions involving these proteins (K_d of human PD-L1/B7-1 ~18.8 μM ; K_d of human PD-1/PD-L1 ~7.8 μM ; K_d of human CD28/B7-1 ~4 μM (28); K_d of human CTLA-4/B7-1 ~0.2 μM (28)). This suggests that B7-1/PD-L1 interactions might have very limited impact. The simulations show, for example, that the expression on T cells of B7-1 (which we were unable to detect) would need to reach a level of >5000 copies/cell (*i.e.* even higher than on mature DCs) in order for the B7-1/PD-L1 interaction to impact PD-1/PD-L1 binding. In the initial study by Butte *et al.* (22), the inhibitory role of the PD-L1/B7-1 interaction was demonstrated by comparing CD28/CTLA-4 double-deficient T cells *versus* CD28/CTLA-4/PD-L1 triple-deficient T cells. Thus the inhibitory role of PD-L1/B7-1 interactions was studied in the absence of “conventional” receptors for B7-1, CTLA-4, and CD28 (*i.e.* in the absence of competition), perhaps exaggerating the physiological importance of B7-1/PD-L1 binding. The effects of this interaction, if any, are likely to be restricted to protein-intrinsic effects on signaling.

REFERENCES

- Nishimura, H., Nose, M., Hiai, H., Minato, N., and Honjo, T. (1999) Development of lupus-like autoimmune diseases by disruption of the PD-1 gene encoding an ITIM motif-carrying immunoreceptor. *Immunity* **11**, 141–151
- Nishimura, H., Okazaki, T., Tanaka, Y., Nakatani, K., Hara, M., Matsumori, A., Sasayama, S., Mizoguchi, A., Hiai, H., Minato, N., and Honjo, T. (2001) Autoimmune dilated cardiomyopathy in PD-1 receptor-deficient mice. *Science* **291**, 319–322
- Ferreiros-Vidal, I., Gomez-Reino, J. J., Barros, F., Carracedo, A., Carreira, P., Gonzalez-Escribano, F., Liz, M., Martin, J., Ordi, J., Vicario, J. L., and Gonzalez, A. (2004) Association of PDCD1 with susceptibility to systemic lupus erythematosus. Evidence of population-specific effects. *Arthritis Rheum.* **50**, 2590–2597
- James, E. S., Harney, S., Wordsworth, B. P., Cookson, W. O., Davis, S. J., and Moffatt, M. F. (2005) PDCD1. A tissue-specific susceptibility locus for inherited inflammatory disorders. *Genes Immun.* **6**, 430–437
- Kong, E. K., Prokunina-Olsson, L., Wong, W. H., Lau, C. S., Chan, T. M., Alarcón-Riquelme, M., and Lau, Y. L. (2005) A new haplotype of PDCD1 is associated with rheumatoid arthritis in Hong Kong Chinese. *Arthritis Rheum.* **52**, 1058–1062
- Barber, D. L., Wherry, E. J., Masopust, D., Zhu, B., Allison, J. P., Sharpe, A. H., Freeman, G. J., and Ahmed, R. (2006) Restoring function in exhausted CD8 T cells during chronic viral infection. *Nature* **439**, 682–687
- Petrovas, C., Price, D. A., Mattapallil, J., Ambrozak, D. R., Geldmacher, C., Cecchinato, V., Vaccari, M., Trzyniszewska, E., Gostick, E., Roederer, M., Douek, D. C., Morgan, S. H., Davis, S. J., Franchini, G., and Koup, R. A. (2007) SIV-specific CD8⁺ T cells express high levels of PD1 and cytokines but have impaired proliferative capacity in acute and chronic SIVmac251 infection. *Blood* **110**, 928–936
- Day, C. L., Kaufmann, D. E., Kiepiela, P., Brown, J. A., Moodley, E. S., Reddy, S., Mackey, E. W., Miller, J. D., Leslie, A. J., DePierres, C., Mncube, Z., Duraiswamy, J., Zhu, B., Eichbaum, Q., Altfeld, M., Wherry, E. J., Coovadia, H. M., Goulder, P. J., Klenerman, P., Ahmed, R., Freeman, G. J., and Walker, B. D. (2006) PD-1 expression on HIV-specific T cells is associated with T-cell exhaustion and disease progression. *Nature* **443**, 350–354
- Radziewicz, H., Ibegbu, C. C., Fernandez, M. L., Workowski, K. A., Obideen, K., Wehbi, M., Hanson, H. L., Steinberg, J. P., Masopust, D., Wherry, E. J., Altman, J. D., Rouse, B. T., Freeman, G. J., Ahmed, R., and Grakoui, A. (2007) Liver-infiltrating lymphocytes in chronic human hepatitis C virus infection display an exhausted phenotype with high levels of PD-1 and low levels of CD127 expression. *J. Virol.* **81**, 2545–2553
- Urbani, S., Amadei, B., Tola, D., Massari, M., Schivazappa, S., Missale, G., and Ferrari, C. (2006) PD-1 expression in acute hepatitis C virus (HCV) infection is associated with HCV-specific CD8 exhaustion. *J. Virol.* **80**, 11398–11403
- Kasprowicz, V., Schulze Zur Wiesch, J., Kuntzen, T., Nolan, B. E., Longworth, S., Berical, A., Blum, J., McMahon, C., Reyor, L. L., Elias, N., Kwok, W. W., McGovern, B. G., Freeman, G., Chung, R. T., Klenerman, P., Lewis-Ximenez, L., Walker, B. D., Allen, T. M., Kim, A. Y., and Lauer, G. M. (2008) High level of PD-1 expression on hepatitis C virus (HCV)-specific CD8⁺ and CD4⁺ T cells during acute HCV infection, irrespective of clinical outcome. *J. Virol.* **82**, 3154–3160
- Francisco, L. M., Salinas, V. H., Brown, K. E., Vanguri, V. K., Freeman, G. J., Kuchroo, V. K., and Sharpe, A. H. (2009) PD-L1 regulates the development, maintenance, and function of induced regulatory T cells. *J. Exp. Med.* **206**, 3015–3029
- Topalian, S. L., Drake, C. G., and Pardoll, D. M. (2012) Targeting the PD-1/B7-H1(PD-L1) pathway to activate anti-tumor immunity. *Curr. Opin. Immunol.* **24**, 207–212
- Yokosuka, T., Takamatsu, M., Kobayashi-Imanishi, W., Hashimoto-Tane, A., Azuma, M., and Saito, T. (2012) Programmed cell death 1 forms negative costimulatory microclusters that directly inhibit T cell receptor signaling by recruiting phosphatase SHP2. *J. Exp. Med.* **209**, 1201–1217
- Keir, M. E., Butte, M. J., Freeman, G. J., and Sharpe, A. H. (2008) PD-1 and its ligands in tolerance and immunity. *Annu. Rev. Immunol.* **26**, 677–704
- Dong, H., Zhu, G., Tamada, K., and Chen, L. (1999) B7-H1, a third member of the B7 family, costimulates T-cell proliferation and interleukin-10 secretion. *Nat. Med.* **5**, 1365–1369
- Freeman, G. J., Long, A. J., Iwai, Y., Bourque, K., Chernova, T., Nishimura, H., Fitz, L. J., Malenkovich, N., Okazaki, T., Byrne, M. C., Horton, H. F., Fouser, L., Carter, L., Ling, V., Bowman, M. R., Carreno, B. M., Collins, M., Wood, C. R., and Honjo, T. (2000) Engagement of the PD-1 immunoinhibitory receptor by a novel B7 family member leads to negative regulation of lymphocyte activation. *J. Exp. Med.* **192**, 1027–1034
- Latchman, Y., Wood, C. R., Chernova, T., Chaudhary, D., Borde, M., Chernova, I., Iwai, Y., Long, A. J., Brown, J. A., Nunes, R., Greenfield, E. A., Bourque, K., Boussiotis, V. A., Carter, L. L., Carreno, B. M., Malenkovich, N., Nishimura, H., Okazaki, T., Honjo, T., Sharpe, A. H., and Freeman, G. J. (2001) PD-L2 is a second ligand for PD-1 and inhibits T cell activation. *Nat. Immunol.* **2**, 261–268
- Tseng, S. Y., Otsuji, M., Gorski, K., Huang, X., Slansky, J. E., Pai, S. I., Shalabi, A., Shin, T., Pardoll, D. M., and Tsuchiya, H. (2001) B7-DC, a new dendritic cell molecule with potent costimulatory properties for T cells. *J. Exp. Med.* **193**, 839–846
- Riley, J. L. (2009) PD-1 signalling in primary T cells. *Immunol. Rev.* **229**, 114–125
- Yu, C., Sonnen, A. F., George, R., Dessailly, B. H., Stagg, L. J., Evans, E. J., Orenco, C. A., Stuart, D. I., Ladbury, J. E., Ikemizu, S., Gilbert, R. J., and Davis, S. J. (2011) Rigid-body ligand recognition drives cytotoxic T-lymphocyte antigen 4 (CTLA-4) receptor triggering. *J. Biol. Chem.* **286**, 6685–6696
- Butte, M. J., Keir, M. E., Phamduy, T. B., Sharpe, A. H., and Freeman, G. J. (2007) Programmed death-1 ligand 1 interacts specifically with the B7-1 costimulatory molecule to inhibit T cell responses. *Immunity* **27**, 111–122
- Butte, M. J., Peña-Cruz, V., Kim, M. J., Freeman, G. J., and Sharpe, A. H. (2008) Interaction of human PD-L1 and B7-1. *Mol. Immunol.* **45**, 3567–3572
- Lin, D. Y., Tanaka, Y., Iwasaki, M., Gittis, A. G., Su, H. P., Mikami, B., Okazaki, T., Honjo, T., Minato, N., and Garboczi, D. N. (2008) The PD-1/PD-L1 complex resembles the antigen-binding Fv domains of antibodies and T cell receptors. *Proc. Natl. Acad. Sci. U.S.A.* **105**, 3011–3016
- Lázár-Molnár, E., Yan, Q., Cao, E., Ramagopal, U., Nathenson, S. G., and

- Almo, S. C. (2008) Crystal structure of the complex between programmed death-1 (PD-1) and its ligand PD-L2. *Proc. Natl. Acad. Sci. U.S.A.* **105**, 10483–10488
26. Springer, T. A. (1991) Cell adhesion. A birth certificate for CD2. *Nature* **353**, 704–705
27. Davis, S. J., Ward, H. A., Puklavec, M. J., Willis, A. C., Williams, A. F., and Barclay, A. N. (1990) High level expression in Chinese hamster ovary cells of soluble forms of CD4 T lymphocyte glycoprotein including glycosylation variants. *J. Biol. Chem.* **265**, 10410–10418
28. Collins, A. V., Brodie, D. W., Gilbert, R. J., Iaboni, A., Manso-Sancho, R., Walse, B., Stuart, D. I., van der Merwe, P. A., and Davis, S. J. (2002) The interaction properties of costimulatory molecules revisited. *Immunity* **17**, 201–210
29. van der Merwe, P. A., Bodian, D. L., Daenke, S., Linsley, P., and Davis, S. J. (1997) CD80 (B7-1) binds both CD28 and CTLA-4 with a low affinity and very fast kinetics. *J. Exp. Med.* **185**, 393–403
30. Veverka, V., Lennie, G., Crabbe, T., Bird, I., Taylor, R. J., and Carr, M. D. (2006) NMR assignment of the mTOR domain responsible for rapamycin binding. *J. Biomol. NMR* **36**, 3
31. Waters, L. C., Böhm, M., Veverka, V., Muskett, F. W., Frenkiel, T. A., Kelly, G. P., Prescott, A., Dosanjh, N. S., Klempnauer, K. H., and Carr, M. D. (2006) NMR assignment and secondary structure determination of the C-terminal MA-3 domain of the tumour suppressor protein Pdc4. *J. Biomol. NMR* **36**, 18
32. Renshaw, P. S., Veverka, V., Kelly, G., Frenkiel, T. A., Williamson, R. A., Gordon, S. V., Hewinson, R. G., and Carr, M. D. (2004) Sequence-specific assignment and secondary structure determination of the 195-residue complex formed by the *Mycobacterium tuberculosis* proteins CFP-10 and ESAT-6. *J. Biomol. NMR* **30**, 225–226
33. Wilkinson, I. C., Hall, C. J., Veverka, V., Shi, J. Y., Muskett, F. W., Stephens, P. E., Taylor, R. J., Henry, A. J., and Carr, M. D. (2009) High resolution NMR-based model for the structure of a scFv-IL-1 β complex. Potential for NMR as a key tool in therapeutic antibody design and development. *J. Biol. Chem.* **284**, 31928–31935
34. Herrmann, T., Güntert, P., and Wüthrich, K. (2002) Protein NMR structure determination with automated NOE assignment using the new software CANDID and the torsion angle dynamics algorithm DYANA. *J. Mol. Biol.* **319**, 209–227
35. Veverka, V., Crabbe, T., Bird, I., Lennie, G., Muskett, F. W., Taylor, R. J., and Carr, M. D. (2008) Structural characterization of the interaction of mTOR with phosphatidic acid and a novel class of inhibitor. Compelling evidence for a central role of the FRB domain in small molecule-mediated regulation of mTOR. *Oncogene* **27**, 585–595
36. Shen, Y., Delaglio, F., Cornilescu, G., and Bax, A. (2009) TALOS+. A hybrid method for predicting protein backbone torsion angles from NMR chemical shifts. *J. Biomol. NMR* **44**, 213–223
37. Güntert, P., and Wüthrich, K. (1991) Improved efficiency of protein structure calculations from NMR data using the program DIANA with redundant dihedral angle constraints. *J. Biomol. NMR* **1**, 447–456
38. Case, D. A., Cheatham, T. E., 3rd, Darden, T., Gohlke, H., Luo, R., Merz, K. M., Jr., Onufriev, A., Simmerling, C., Wang, B., and Woods, R. J. (2005) The Amber biomolecular simulation programs. *J. Comput. Chem.* **26**, 1668–1688
39. Tsui, V., and Case, D. A. (2000) Molecular dynamics simulations of nucleic acids using a generalized Born solvation model. *J. Am. Chem. Soc.* **122**, 2489–2498
40. Koradi, R., Billeter, M., and Wüthrich, K. (1996) MOLMOL. A program for display and analysis of macromolecular structures. *J. Mol. Graph.* **14**, 51–55, 29–32
41. Davis, I. W., Leaver-Fay, A., Chen, V. B., Block, J. N., Kapral, G. J., Wang, X., Murray, L. W., Arendall, W. B., 3rd, Snoeyink, J., Richardson, J. S., and Richardson, D. C. (2007) MolProbity. All-atom contacts and structure validation for proteins and nucleic acids. *Nucleic Acids Res.* **35**, W375–W383
42. DeLano, W. L. (2010) *The PyMOL Molecular Graphics System*, version 1.3r1, Schrodinger, LLC, New York
43. Farmer, B. T., Constantine, K. L., Goldfarb, V., Friedrichs, M. S., Wittekind, M., Yanchunas, J., Robertson, J. G., and Mueller, L. (1996) Localizing the NADP⁺ binding site on the MurB enzyme by NMR. *Nat. Struct. Mol. Biol.* **3**, 995–997
44. Muskett, F. W., Frenkiel, T. A., Feeney, J., Freedman, R. B., Carr, M. D., and Williamson, R. A. (1998) High resolution structure of the N-terminal domain of tissue inhibitor of metalloproteinases-2 and characterization of its interaction site with matrix metalloproteinase-3. *J. Biol. Chem.* **273**, 21736–21743
45. Williamson, R. A., Carr, M. D., Frenkiel, T. A., Feeney, J., and Freedman, R. B. (1997) Mapping the binding site for matrix metalloproteinase on the N-terminal domain of the tissue inhibitor of metalloproteinases-2 by NMR chemical shift perturbation. *Biochemistry* **36**, 13882–13889
46. Evans, E. J., Castro, M. A., O'Brien, R., Kearney, A., Walsh, H., Sparks, L. M., Tucknott, M. G., Davies, E. A., Carmo, A. M., van der Merwe, P. A., Stuart, D. I., Jones, E. Y., Ladbury, J. E., Ikemizu, S., and Davis, S. J. (2006) Crystal structure and binding properties of the CD2 and CD244 (2B4)-binding protein, CD48. *J. Biol. Chem.* **281**, 29309–29320
47. Evans, E. J., Esnouf, R. M., Manso-Sancho, R., Gilbert, R. J., James, J. R., Yu, C., Fennelly, J. A., Vowles, C., Hanke, T., Walse, B., Hüning, T., Sørensen, P., Stuart, D. I., and Davis, S. J. (2005) Crystal structure of a soluble CD28-Fab complex. *Nat. Immunol.* **6**, 271–279
48. Wiseman, T., Williston, S., Brandts, J. F., and Lin, L. N. (1989) Rapid measurement of binding constants and heats of binding using a new titration calorimeter. *Anal. Biochem.* **179**, 131–137
49. Ladbury, J. E., and Chowdhry, B. Z. (1996) Sensing the heat. The application of isothermal titration calorimetry to thermodynamic studies of biomolecular interactions. *Chem. Biol.* **3**, 791–801
50. Jansson, A., Barnes, E., Klenerman, P., Harlén, M., Sørensen, P., Davis, S. J., and Nilsson, P. (2005) A theoretical framework for quantitative analysis of the molecular basis of costimulation. *J. Immunol.* **175**, 1575–1585
51. Jansson, A., and Davis, S. J. (2011) Quantitative analysis predicts the relative therapeutic efficacy of different forms of CTLA4Ig. *Mol. Immunol.* **49**, 527–536
52. Holm, L., and Park, J. (2000) DaliLite workbench for protein structure comparison. *Bioinformatics* **16**, 566–567
53. Zhang, X., Schwartz, J. C., Guo, X., Bhatia, S., Cao, E., Lorenz, M., Cammer, M., Chen, L., Zhang, Z. Y., Edidin, M. A., Nathenson, S. G., and Almo, S. C. (2004) Structural and functional analysis of the costimulatory receptor programmed death-1. *Immunity* **20**, 337–347
54. Saunders, P. A., Hendrycks, V. R., Lidinsky, W. A., and Woods, M. L. (2005) PD-L2:PD-1 involvement in T cell proliferation, cytokine production, and integrin-mediated adhesion. *Eur. J. Immunol.* **35**, 3561–3569
55. Dong, H., Strome, S. E., Matteson, E. L., Moder, K. G., Flies, D. B., Zhu, G., Tamura, H., Driscoll, C. L., and Chen, L. (2003) Costimulating aberrant T cell responses by B7-H1 autoantibodies in rheumatoid arthritis. *J. Clin. Invest.* **111**, 363–370
56. Bell, G. I. (1978) Models for the specific adhesion of cells to cells. *Science* **200**, 618–627
57. Prabhu Das, M. R., Zamvil, S. S., Borriello, F., Weiner, H. L., Sharpe, A. H., and Kuchroo, V. K. (1995) Reciprocal expression of co-stimulatory molecules, B7-1 and B7-2, on murine T cells following activation. *Eur. J. Immunol.* **25**, 207–211
58. Sansom, D. M., and Hall, N. D. (1993) B7/BB1, the ligand for CD28, is expressed on repeatedly activated human T cells *in vitro*. *Eur. J. Immunol.* **23**, 295–298
59. Azuma, M., Yssel, H., Phillips, J. H., Spits, H., and Lanier, L. L. (1993) Functional expression of B7/BB1 on activated T lymphocytes. *J. Exp. Med.* **177**, 845–850
60. Stamper, C. C., Zhang, Y., Tobin, J. F., Erbe, D. V., Ikemizu, S., Davis, S. J., Stahl, M. L., Sehra, J., Somers, W. S., and Mosyak, L. (2001) Crystal structure of the B7-1/CTLA-4 complex that inhibits human immune responses. *Nature* **410**, 608–611
61. Parry, R. V., Chemnitz, J. M., Frauwirth, K. A., Lanfranco, A. R., Braunstein, I., Kobayashi, S. V., Linsley, P. S., Thompson, C. B., and Riley, J. L. (2005) CTLA-4 and PD-1 receptors inhibit T-cell activation by distinct mechanisms. *Mol. Cell Biol.* **25**, 9543–9553
62. Schneider, H., Downey, J., Smith, A., Zinselmeyer, B. H., Rush, C., Brewer, J. M., Wei, B., Hogg, N., Garside, P., and Rudd, C. E. (2006) Reversal of the TCR stop signal by CTLA-4. *Science* **313**, 1972–1975

63. Qureshi, O. S., Zheng, Y., Nakamura, K., Attridge, K., Manzotti, C., Schmidt, E. M., Baker, J., Jeffery, L. E., Kaur, S., Briggs, Z., Hou, T. Z., Futter, C. E., Anderson, G., Walker, L. S., and Sansom, D. M. (2011) Trans-endocytosis of CD80 and CD86. A molecular basis for the cell-extrinsic function of CTLA-4. *Science* **332**, 600–603
64. Dong, H., Zhu, G., Tamada, K., Flies, D. B., van Deursen, J. M., and Chen, L. (2004) B7-H1 determines accumulation and deletion of intrahepatic CD8⁺ T lymphocytes. *Immunity* **20**, 327–336
65. Shin, T., Yoshimura, K., Shin, T., Crafton, E. B., Tsuchiya, H., Housseau, F., Koseki, H., Schulick, R. D., Chen, L., and Pardoll, D. M. (2005) *In vivo* costimulatory role of B7-DC in tuning T helper cell 1 and cytotoxic T lymphocyte responses. *J. Exp. Med.* **201**, 1531–1541